Precambrian Research 353 (2021) 106039

Contents lists available at ScienceDirect

Precambrian Research

journal homepage: www.elsevier.com/locate/precamres

New constraints for paleogeographic reconstructions at *ca.* 1.88 Ga from geochronology and paleomagnetism of the Carajás dyke swarm (eastern Amazonia)

P.Y.J. Antonio [a,b,*], M.S. D'Agrella-Filho [a], A. Nédélec [b], M. Poujol [c], C. Sanchez [d], E.L. Dantas [e], R. Dall'Agnol [f,g], M.F.B. Teixeira [h], A. Proietti [i], C.I. Martínez Dopico [j], D.C. Oliveira [f], F.F. Silva [f], B. Marangoanha [f], R.I.F. Trindade [a]

[a] *Instituto de Astronomia, Geofísica e Ciências Atmosféricas (IAG), Universidade de São Paulo (USP), Rua do Matão, 1226, 05508-090 São Paulo, SP, Brazil*
[b] *Géosciences Environnement Toulouse (GET), Université de Toulouse, UPS, CNRS, IRD, CNES, 14 Avenue E. Belin, 31400 Toulouse, France*
[c] *Géosciences Rennes, UMR CNRS 6118, Université Rennes 1, 35042 Rennes Cedex, France*
[d] *GEOPS, Université Paris-Sud, CNRS, Université Paris-Saclay, Rue du Belvédère, Bât. 504, 91405 Orsay, France*
[e] *Instituto de Geociências, Universidade de Brasília, ICC-Centro, Campus Universitário Darcy Ribeiro Asa Norte, 70910-900 Brasilia, DF, Brazil*
[f] *Instituto de Geociências (IG), Universidade Federal do Pará (UFPA), CEP-66075-900 Belém, Pará, Brazil*
[g] *Instituto Tecnologico Vale, Belém, Pará, Brazil*
[h] *Universidade Federal do Oeste do Pará, Santarém, Pará, Brazil*
[i] *Centre de Microcaractérisation Raimond Castaing, 3 Rue Caroline Aigle, 31400 Toulouse, France*
[j] *Institute of Geochronology and Isotope Geology (INGEIS, CONICET), University of Buenos Aires, Argentina*

ARTICLE INFO

Keywords:
Amazonia
West Africa
Paleogeography
Paleomagnetism
Uatumã
Carajás

ABSTRACT

The Uatumã event is a silicic large igneous province (SLIP) covering an area of 1.500.000 km^2 of the Amazonia craton at *ca.* 1890–1850 Ma. New paleomagnetic data and U-Pb apatite ages for coeval microgranitic, andesitic, and basaltic dykes in the Carajás Province (southeastern Amazonia craton) are presented. Two primary characteristic remanent magnetizations (ChRMs) were isolated for the Carajás dykes which were combined with published results for coeval rocks in the São Felix do Xingu area, producing two grand mean poles: (1) "CA1", dated at 1880 Ma on zircon and apatite, whose mean site directions cluster around the mean $D_m = 132.8°$, $I_m = 76°$ ($N = 26$, $\alpha_{95} = 5°$, $k = 32.7$), yielding the paleomagnetic pole at 328.7°E, 23.3°S, ($A_{95} = 8.7°$ $K = 11.7$), and (2) "CA2" from well-dated microgranitic dykes of the Velho Guilherme Suite (1855 Ma U-Pb on zircon and apatite). Site mean directions group around the mean $D_m = 240.3°$, $I_m = 11.8°$ ($N = 18$, $\alpha_{95} = 10.8°$, $k = 11.1$), which yielded the paleomagnetic pole at 221.3°E, 30.2°S, ($A_{95} = 8.8°$, $K = 16.2$). The remanent magnetization of the Velho Guilherme microgranitic dykes is carried by pseudo-single domain (PSD) magnetite. Its primary origin is supported by a positive baked contact test. Two younger secondary components were also isolated in the Carajás dyke swarm: one probably associated to the Mesozoic Central Atlantic magmatic province (CD3), and another component (CD4) with yet undefined age. A new configuration for the Amazonia and West Africa during the Paleoproterozoic, which aligns the Sassandra shear zone (in Africa) and the North Guiana Through and other shear zones (in Guiana Shield), is supported by geological and paleomagnetic data. The large angular distance between the 1880 Ma CA1 and 1855 Ma CA2 ($Q \sim 6$) poles that are relatively close in age implies in a high plate velocity for the Amazonia craton, which is not consistent with modern plate tectonics. A similar large discrepancy between 1880 and 1860 Ma poles was also observed at least as many as six cratons. Although other hypotheses can be invoked, such as non-uniformitarian magnetic fields, the occurrence of large-scale true polar wander at this time may be the most parsimonious explanation of the widespread discrepancies.

* Corresponding author.
E-mail address: paulantonio0931@gmail.com (P.Y.J. Antonio).

https://doi.org/10.1016/j.precamres.2020.106039
Received 21 April 2020; Received in revised form 11 September 2020; Accepted 18 November 2020
Available online 17 December 2020

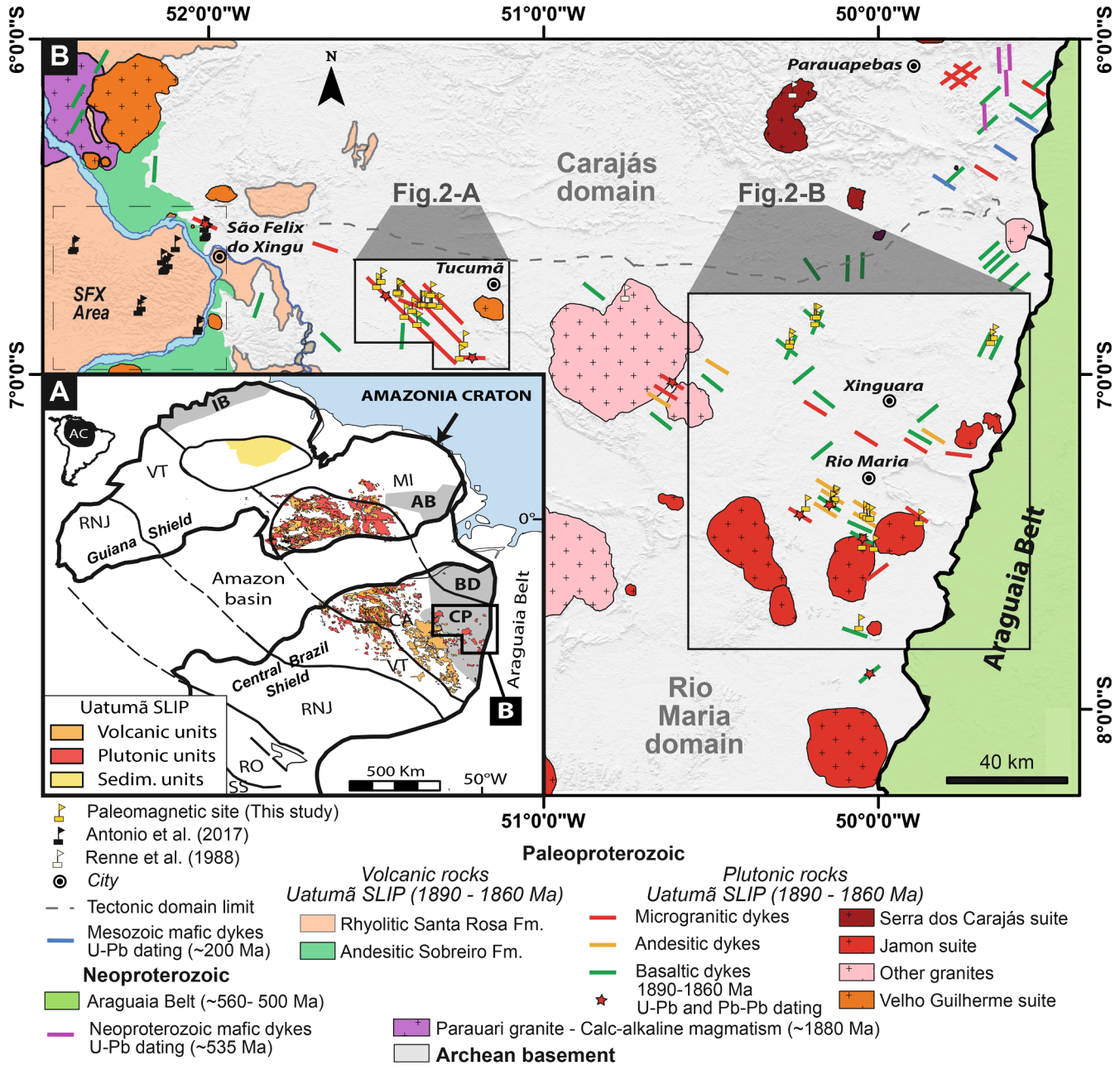

Fig. 1. A: Inset of the ~1880–1860 Ma volcano-plutonic Uatumã SLIP (silicic large igneous province) and the main tectonic provinces of the Amazonia craton (adapted from Cordani and Teixeira (2007)). *Abbreviations*: Archean blocks are represented in grey: *CP* = Carajás Province, BD = Bacajá domain, IB = Imataca Block, AM = Amapá Block; CA = Central Amazonia Province MI = Maroni-Itacaiunas Province; VT = Ventuari-Tapájos Province; RNJ = Rio Negro-Juruena Province; RO = Rondonian-San Ignácio Province; SS = Sunsás province,. B: The 1.88 Ga Uatumã SLIP in the Carajás Province. The geological maps of the Tucumã and Rio Maria areas represented in Fig. 2 are indicated. These areas belong to the Rio Maria tectonic domain (southern) which is separated of the Carajás tectonic domain by the dashed line. Localization of paleomagnetic sites of this study, sites published in Antonio et al. (2017) (SFX area), and sites of Renne et al. (1988) are indicated. U-Pb and Pb-Pb dating for dykes are referred to Teixeira et al. (2019b).

1. Introduction

Geodynamics during Proterozoic times in relation to the Earth's thermal evolution and convection remains a challenging task to elucidate (Ernst, 2017). After the probable onset for plate tectonics during the Archean at *ca.* 3200 Ma (Shirey and Richardson, 2011), the Paleoproterozoic eon is marked by a transitional period between the Archean stagnant-lid tectonics and the mobile-lid tectonics (Brown et al., 2020; Liu et al., 2019). In that sense, paleogeographic reconstructions are keystone to understand the Earth's geodynamics. The relative positions of cratons are mostly based mainly on correlations of geological records (orogenic sutures, dyke swarms, similarities between lithologies, *etc.*) and can only be properly constrained with the acquisition of high-quality paleomagnetic poles for each craton, in order to precisely provide their apparent polar wander paths (APWPs) (Buchan, 2013). In addition, since the beginning of the Paleoproterozoic, Earth history was punctuated by quasi-periodic supercontinental cycles where larger landmasses or supercontinents were formed in specific time intervals (Condie, 1998; 2002;; Condie and Aster, 2013; Murphy, 2013; Nance et al., 1988, 2014; Nance and Murphy, 2013; Worsley et al., 1984). A large consensus exists for the best-defined supercontinents: such as Pangea at *ca.* 350–200 Ma (Domeier et al., 2012; Stampfli et al., 2013)

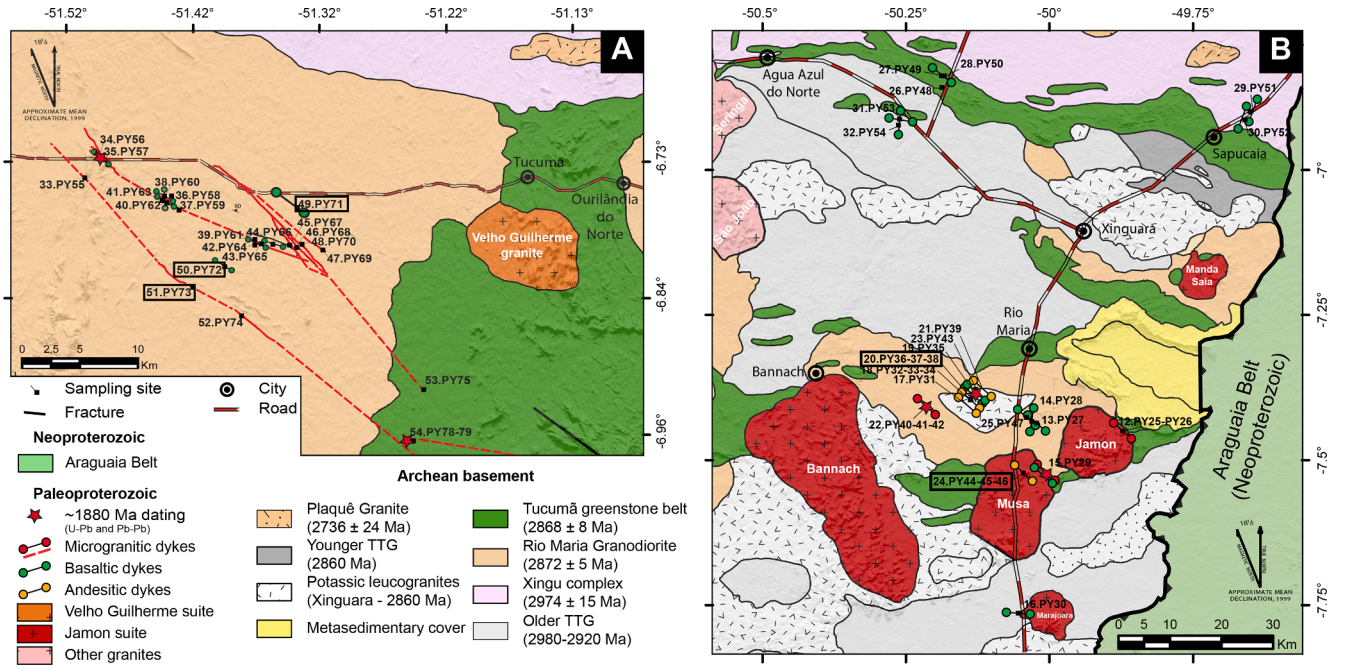

Fig. 2. Geological maps of Tucumã (2-A) and Rio Maria (2-B) areas with localization of sampling sites, modified from Vasquez et al. (2008). See Fig. 1 for areas localities in the Carajás Province and supplementary data 1 for the GPS coordinates of dykes. Selected sites for U-Pb geochronology in this study are indicated with a surrounding frame.

and Rodinia at *ca.* 1100–750 Ma (Li et al., 2013; Merdith et al., 2017). The first Proterozoic supercontinent in Earth's history (at *ca.* 1800–1600 Ma), hereafter called Columbia (a.k.a. Nuna) according to Meert (2012), is the subject of debates regarding its configuration during the Paleo-Mesoproterozoic times (D'Agrella-Filho et al., 2016; Evans and Mitchell, 2011; Evans, 2013; Evans et al., 2016; Johansson, 2009; Meert and Santosh, 2017; Pehrsson et al., 2016; Pisarevsky et al., 2014; Zhang et al., 2012). The main geological evidence for the existence of Columbia is the presence of 2100 to 1800 Ma orogeneses that have been described in most cratons, suggesting growth of large landmasses (Zhao et al., 2002, 2004). This period of amalgamation was considered as a "turmoil" by Antonio et al. (2017), and preceded one interval between 1800 and 800 Ma, the so-called "boring billion", where no changes are observed in the atmosphere and ocean compositions (Roberts, 2013). It is widely accepted that Laurentia was not completely assembled at *ca.* ~1900 Ma, and large distances existed between its cratons (Slave, Rae, Hearne, Nain, Wyoming and Superior) (Kilian et al., 2016). Final suturing for Baltica resulted from the collision between Fennoscandia and the Volgo-Sarmatia block at *ca.* 1750 Ma, along the Svecofennian orogeny, which implies these cratonic blocks were separated at *ca.* 1880 Ma (Bogdanova et al., 2013, 2016; Lubnina et al., 2016).

The present study addresses the reconstruction of the Amazonia craton during the Paleoproterozoic, one of the major pieces of the Columbia jigsaw. The Amazonia craton is considered to have been linked to West Africa at *ca.* 1960 Ma after the ~2000 Ma Trans-Amazonian/Eburnean Orogeny (Bispo-Santos et al., 2014a; D'Agrella-Filho et al., 2016; Nomade et al., 2003; Onstott and Hargraves, 1981; Onstott et al., 1984b; Théveniaut et al., 2006). A geological link with Baltica was supported by paleomagnetic data including the Amazonia craton in the core of Columbia connection at latest Paleoproterozoic, at *ca.* 1790 Ma (Bispo-Santos et al., 2014b). The Amazonia and West Africa cratons were also considered as an isolated large landmasses drifting separated from Columbia (Pisarevsky et al., 2014).

Anomalous paleomagnetic data were reported for cratons during the Columbia supercontinent assembly (2000–1800 Ma) which was interpreted as the consequence of either rapid plate motions, absence of a stable dipolar field, tectonic problems, or true polar wander (TPW) events (Hanson et al., 2004, 2011; McGlynn and Irving, 1978; Mitchell et al., 2010; Mitchell, 2014). A comprehensive compilation of available paleomagnetic data at *ca.* 1890–1860 Ma supports the existence of a TPW event linked to the reorganization of whole mantle convection (Antonio et al. (2017). This TPW event was coeval with the widespread occurrence of large igneous provinces (LIPs) in most cratons worldwide (Isley and Abbott, 1999). Emplacement of LIPs implies the existence of large plumbing systems with layered intrusions, sills provinces and giant dyke swarms providing possibilities to reconstruct older cratonic associations using the LIP records from different cratons (Bleeker, 2003; Ernst et al., 2010, 2013; Söderlund et al., 2016).

Preliminary paleomagnetic investigations in the Carajás Province was performed by Renne et al. (1988) on nine specimens (2 sites in Fig. 1). Here we present new paleomagnetic and geochronological results for the Tucumã and Rio Maria dyke swarms in Pará state, southern Amazonia craton. Compared with paleomagnetic data obtained on associated volcanic rocks of the ~1890–1860 Ma Uatumã SLIP (silicic large igneous province) by Antonio et al. (2017), these new key poles have large implications for Precambrian geodynamics.

2. Geological setting and lithology

2.1. The Uatumã SLIP

The Amazonia craton is one of the largest cratons of the world with ~4.400.000 km^2 (Almeida et al., 1981). It consists of the Guiana Shield in the north and the Central-Brazil (or Guaporé) Shield in the south, separated by the Amazon sedimentary basin (Santos et al., 2000; Schobbenhaus et al., 1984) (Fig. 1-A). In the Guiana Shield, two major Archean nuclei have been recognized, the Imataca Block in northern part and the Amapá Block in the eastern part (Rosa-Costa et al., 2006; Tassinari et al., 2004). In the Central-Brazil Shield, the Archean portion is composed of the Carajás Province and the Bacajá Block (Vasquez et al., 2008). Except for the Carajás Province, these Archean nuclei were reworked during the Transamazonian/Eburnean orogeny, which main area of influence is largely coincident with the geochronological Maroni-Itacaiunas Province (2260–1950 Ma) (Cordani and Teixeira, 2007). The

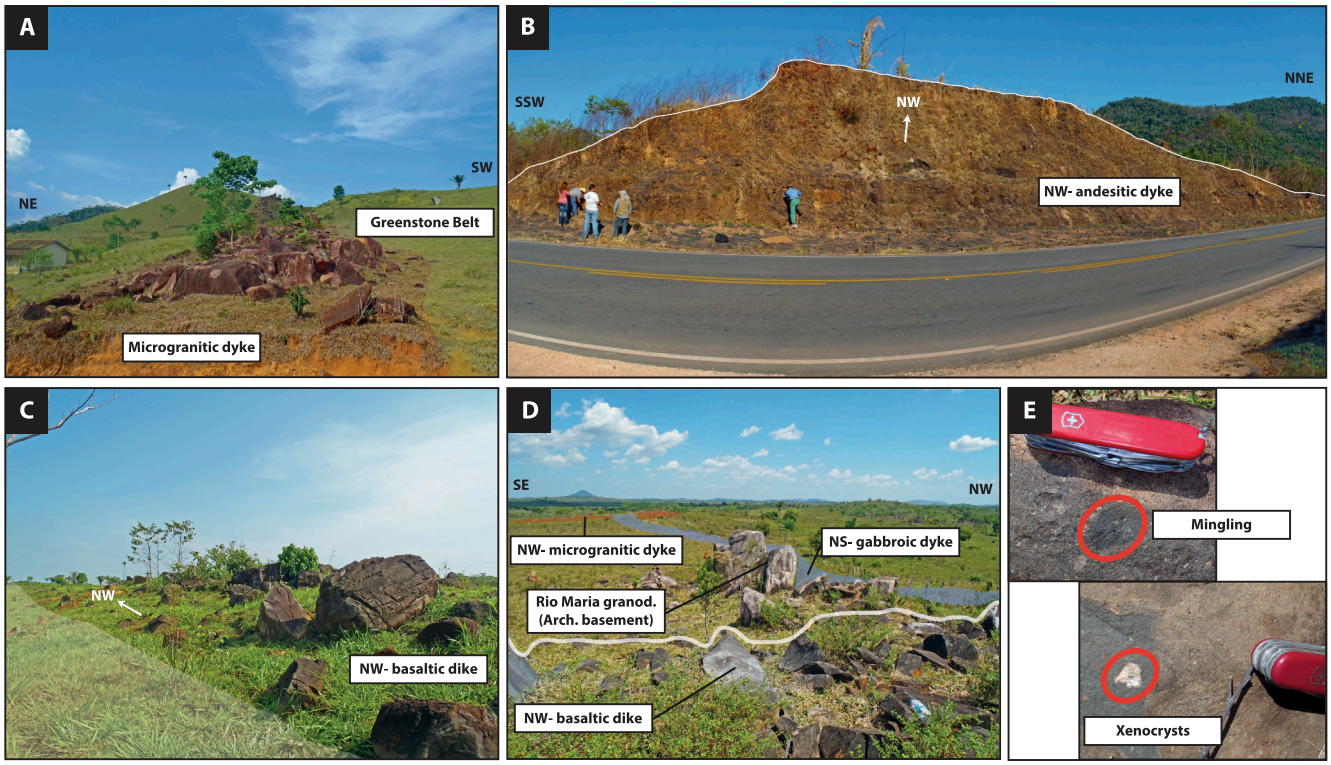

Fig. 3. Outcrops photos of the Carajás dyke swarm. A: 1880 Ma microgranitic dyke, ~6 m in width (Site 54), intruding the Archean greenstone belt (in green). B: Cross-sectional view for a ~1880 Ma andesitic dyke (Site 24). White line is the boundary of the dyke and people give the scale, ~25 m in width. C: ~1880 Ma NW-trending basaltic dyke with typical isolated blocks, ~5 m in width (Site PY49). D: Field relationship where a NS- Mesozoic dyke crosscuts NW- trending microgranitic and basaltic dykes. Archean granodiorite Rio Maria is visible (Site 38). E: Field evidences of mingling (mafic enclave in microgranitic dyke) and xenocrysts (K-feldspar in basaltic dyke) (Site 34). (For interpretation of the references to color in this figure legend, the reader is referred to the web version of this article.)

Carajás Province is the oldest crustal portion of the stable Archean-Paleoproterozoic core of the Amazonia craton, the Central Amazonian Province (Tassinari and Macambira, 2004; Teixeira et al., 2019b). During the Paleoproterozoic times, accretionary belts occurred along the southwestern margin of this cratonized landmass with the development among others of the Ventuari – Tapajós Province (2000–1800 Ma) (Bettencourt et al., 2016; Valério et al., 2018).

The Carajás Province comprises the Carajás (north) and Rio Maria (south) tectonic domains, and is delimited to the east by the Araguaia Belt (~550 Ma) (Fig. 1-B) (Santos, 2003; Silva et al., 1974; Vasquez et al., 2008). These domains were intruded by the ~1900–1850 Ma rocks of the Uatumã event (Amaral, 1974), which form a silicic large igneous province (SLIP) (Fig. 1-A-B) (Dall'Agnol et al., 2005; Dall'Agnol and Oliveira, 2007; Giovanardi et al., 2019; Rivalenti et al., 1998; Silva et al., 1999; Teixeira et al., 2018, 2019b). This SLIP is considered as one of the largest continental magmatic event of the Earth's history (>1.500.000 km^2) (Ernst, 2014). In the studied area, it is composed of Paleoproterozoic anorogenic granites (Jamon, Serra dos Carajás and Velho Guilherme suites and similar related granites) with associated dykes in the Rio Maria and Tucumã areas, and by felsic to intermediate volcanic and plutonic rocks (São Felix do Xingu area) (Fig. 1), which were dated between 1890 and 1860 Ma (Antonio et al., 2017; Teixeira et al., 2019b). These Paleoproterozoic units are well-preserved without deformation and no younger orogenic event is recorded into the Carajás Province.

The origin of the Uatumã SLIP involves mafic underplating and the emplacement of giant dyke swarms associated with crustal extension (Dall'Agnol et al., 1994; Giovanardi et al., 2019; Silva et al., 2016). Thermal perturbations in association with a plume activity were also related to a true polar wander event induced by geoidal perturbations (Antonio et al., 2017). An alternative origin of this magmatism considers that the south-western side of the Central Amazonian Province was affected by a flat-subduction period followed by a slab break-off in an arc-related environment (Cassini et al., 2020; Fernandes et al., 2011; Juliani and Fernandes, 2010; Roverato et al., 2019).

2.2. Carajás dyke swarm

In this study, we sampled mafic and felsic dykes (Carajás dyke swarm) crosscutting the Archean basement of the Carajás Province, to the east of the coeval volcanic units (São Felix do Xingu, SFX) previously studied by Antonio et al. (2017) (Fig. 1-B). Two areas with dyke intrusions in the Rio Maria domain were the targets of this paleomagnetic study, the Tucumã (Fig. 2-A) and the Rio Maria (Fig. 2-B) areas. Near to Tucumã city, the NW- trending dyke swarm is located to the west of the ~1860 Ma A-type Velho Guilherme granite and intrudes the Archean Rio Maria granodiorite dated at 2872 ± 5 Ma by U-Pb on zircon (Pimentel and Machado, 1994) and the Tucumã greenstone belt dated at 2868 ± 8 Ma by Pb-Pb evaporation on zircon (Avelar et al., 1999) (Fig. 2-A). Near to Rio Maria city, the dykes are associated to the ~1880 Ma Jamon suite and intrude a complex Mesoarchean juvenile crust composed by sequences of greenstone belts, TTG series and sanukitoid-rocks (3000–2860 Ma) (Fig. 2-B). The Jamon suite and related granites are well-dated by U-Pb (TIMS) on zircons with ages between 1880 and 1857 Ma (Teixeira et al., 2018), and their magmas derived essentially by crustal anatexis of Archean protoliths (Teixeira et al., 2019a). According to the U-Pb ages of felsic and mafic dykes, three generations of dykes are recognized in the Carajás Province: (1) The *ca.* 1880 Ma Carajás dykes (*i.e.*, the Uatumã SLIP), (2) the *ca.* 535 Ma Parauapebas dykes, and (3) the Mesozoic dykes associated to the Central Atlantic Magmatic Province (CAMP) (Antonio et al., 2017; Silva et al., 2016; Teixeira et al., 2019b).

2.2.1. The 1880 Ma Carajás dykes

The *ca.* 1880 Ma Carajás dykes include (i) NW- trending

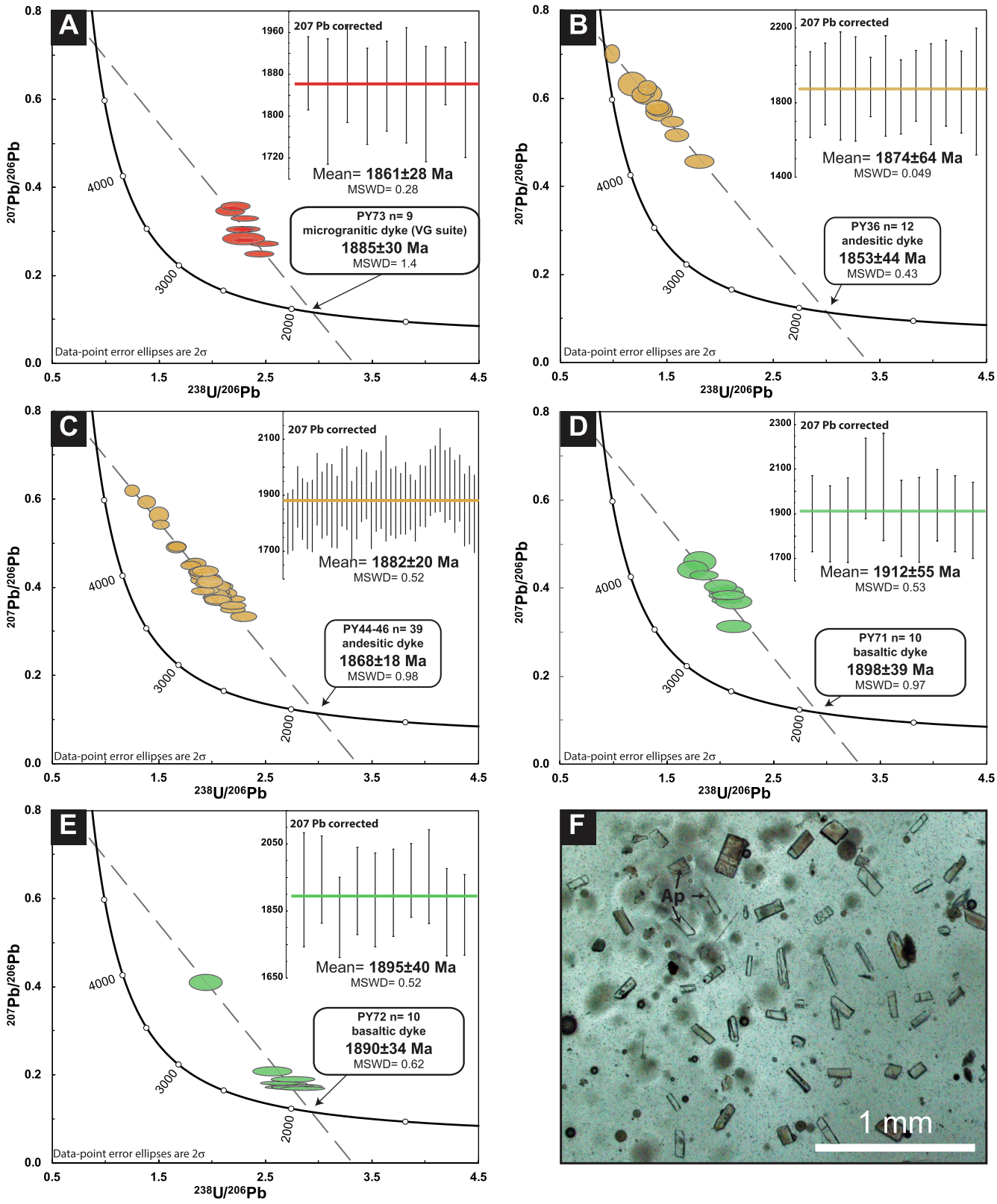

Fig. 4. Tera-Wasserburg Concordia diagram of apatite analyses with the corresponding ^{207}Pb corrected age for one microgranitic dyke (A), two andesitic dykes (B-C), two basaltic dykes (D-E) from the Carajás dyke swarm. F: Photomicrograph of apatite crystals in binocular microscopy. ^{207}Pb/^{206}Pb value of 0.990 was calculated following the Pb evolution model of Stacey and Kramers (1975).

microgranitic (or rhyolitic) dykes which likely represent the subvolcanic equivalent of the A-type granites in the Carajás Province, (ii) NW-trending andesitic dykes, and (iii) NW- and NE-trending basaltic dykes.

The NW- trending microgranitic dykes are subvertical, *ca.* 15 m in width and a few hundred meters in length in average (Fig. 3-A). They are made of A-type subsolvus microgranite characterized by subhedral phenocrysts of quartz, alkali feldspar and plagioclase in a quartz-feldspar matrix with granophyric texture. The most frequently observed primary accessory minerals are zircon, titanite and magnetite. In the Tucumã are, two of these microgranitic dykes were dated by SHRIMP U-Pb on zircon, which revealed ages of 1882 ± 4 Ma and 1881 ± 3 Ma (Silva et al., 2016). Pb-Pb evaporation ages for these microgranitic dykes in the Rio Maria area indicate an emplacement between 1890 and 1870 Ma (Oliveira, 2006; Rodrigues et al., 2015). U-Pb ages of 1895 ± 11 Ma and 1854 ± 6 Ma for microgranitic dykes in the western part (São Felix do Xingu area) of the Carajás Province show that this NW-trending dyke swarm extends for ~300 km in length between Rio Maria and São Felix do Xingu (Antonio et al., 2017).

The NW- trending **andesitic dykes** are observed mainly in the Rio Maria area (Fig. 3-B) and rarely in the northern Carajás and Tucumã areas (Rivalenti et al., 1998). They have a porphyritic texture with plagioclase phenocrysts. Groundmass is constituted by quartz, plagioclase, altered clinopyroxene, and Fe-Ti oxides. Andesitic dykes have a high-K calc-alkaline character (Rivalenti et al., 1998). A Rb-Sr isochron for andesites defines a poorly constrained age of 1874 ± 110 Ma (Rivalenti et al., 1998), which suggests that these andesitic dykes could be coeval with the ~1880 Ma microgranitic dykes.

The NW- and NE- trending **basaltic dykes** are tholeiitic in composition with ophitic texture (Fig. 3-C). A baddeleyite U-Pb age of 1880 ± 1.5 Ma was recently published for a NW- basaltic dyke from the Rio Maria area (Teixeira et al., 2019b). Another baddeleyite U-Pb age of 1884.6 ± 1.6 Ma obtained for a NE- trending dyke supports the idea that these basaltic dyke are coeval with the microgranitic and andesitic dykes (Teixeira et al., 2019b). The occurrence of composite NW-trending basaltic and microgranitic dykes and showing basaltic enclave in the microgranitic dyke and dropped K-feldspar megacrysts in the basaltic rocks (site 34) are substantial field evidences to indicate a coeval emplacement of these dykes (Fig. 3-E). Similar features were also observed in site 15 (Fig. 2-B) near the northeastern border of the Musa pluton cutting the Rio Maria granodiorite (Dall'Agnol et al., 2006).

2.2.2. *Younger generations of dykes in Carajás*

Two younger events of basaltic dykes were recognized in the Carajás Province. Near to Parauapebas (Fig. 1-B), a new baddeleyite U-Pb age of 531 ± 1 Ma for a NS- trending basaltic dyke demonstrate the existence of Neoproterozoic dykes in the region (Teixeira et al., 2012b, 2019b). These Parauapebas dykes may represent a post-collisional extension at the southeastern margin of the craton in response to the Neoproterozoic Araguaia Belt (Teixeira et al., 2019b). A baddeleyite U-Pb age of 199 ± 0.3 Ma for a basaltic dyke in northern Carajás indicates the presence of Mesozoic dykes in the region (Teixeira et al., 2012a, 2019b). These dykes can be related to the ~200 Ma Central Atlantic Magmatic Province (CAMP) in Brazil (De Min et al., 2003). Mesozoic dykes are also observed in Tucumã where a gabbroic dyke crosscuts the microgranite and basaltic dykes of the Uatumã SLIP (Fig. 3-D).

3. Sampling and laboratory procedures

3.1. Sampling

The Paleoproterozoic dyke swarm of the Uatumã SLIP was sampled for a paleomagnetic study in the Tucumã and Rio Maria areas (GPS location in Supplementary data 1). In the Tucumã area we sampled 28 sites thus distributed: (i) 16 NW- trending microgranitic dykes from the well-dated ~1880 Ma swarm (sites 33, 34, 36, 37, 39, 40, 41, 43, 45, 46, 47, 48, 51, 52, 53 and 54), (ii) 7 NW- trending basaltic dykes with evidence for mingling with the microgranitic dykes (sites 35, 38, 40, 42, 44, 49 and 50), (iii) 2 sites for one NS- trending gabbroic dyke which is considered to be Mesozoic in age (sites 38 and 41) given its freshness and crosscutting relations, and (iv) 3 sites of Archean basement for a baked contact test, and to test regional consistency (sites 36, 38 and 46) (Fig. 2-A;). In the Rio Maria area we sampled 25 sites thus distributed: (i) 2 NW-trending microgranitic dykes dated at ~1880 Ma (sites 12 and 22) and a felsic part of a composite dyke (site 15), (ii) 5 NW- trending andesitic dykes of ~1880 Ma (sites 17, 18, 20, 21 and 24), (iii) 8 NW- trending basaltic dykes, one of which (site 19) is well-dated (U-Pb on baddeleyite) at ~1880 Ma (sites 13, 19, 15, 16, 23, 25, 27 and 31), (iv) 6 NE- trending basaltic dykes that we assume to be Mesozoic in age (sites 14, 26, 28, 29, 30 and 32), and (v) 4 sites of Archean basement rocks for a baked contact test (Sites 14, 16, 17 and 22) (Fig. 2-B). A total of 304 cylindrical cores (~2.54 cm in diameter) and 15 oriented block samples were collected in both areas and oriented with a magnetic compass, and in most cases, also using a solar compass.

As rocks are often poorly exposed in these areas, most dykes were sampled on isolated blocks, without certainty of their *in-situ* position (Fig. 3). However, consistent paleomagnetic results were obtained intra and inter-sites (see below), which confirm that the sampled blocks suffered very small movements. Furthermore, it was difficult to observe the direct lithological contacts in these challenging outcrops (weathering, mature soils). Nevertheless, in the Tucumã area we attempted a contact test between the Mesozoic gabbroic dyke and a NW- microgranitic dyke (Fig. 9-A). In the Rio Maria area, direct contacts with the country rock are not visible, and dykes generally crop out as isolated blocks, so that, no adequate baked contact test could be realized. Whenever possible, however, we collected 'in situ' Archean rocks trying to isolate the magnetic direction carried by the country rocks. We sampled Archean rocks close to a NW- microgranitic dyke (site 22), close to a NW-andesitic dyke (site 17), close to a NW- basaltic dyke (site 16) and close to a NE- basaltic dyke (site 14). We sampled also the basaltic-felsic composite dyke dated at ~1880 Ma (Oliveira, 2006) (site 15). Trying to best support the paleomagnetic data, selected rocks were prepared for U-Pb analysis on apatite and zircon grains.

3.2. Geochronology

The sample preparation for the apatite and zircon separation was performed in the Geosciences Environnement Toulouse laboratory (GET, Toulouse, France). The freshest part of the rock cylinders as well as hand samples were crushed and sieved to collect the mineral fraction below 400 μm. The ultra-fine sized mineral fractions (as the clay) and the low-density minerals were removed with a Wilfley table. Heavy minerals were then isolated using heavy liquids (tetrabromoethane and diiodomethane, with respective densities of 2.967 and 3.325). Magnetic minerals were consequently removed with a Franz magnetic separator. Then, the apatite and zircon grains were handpicked with a binocular microscope before being mounted in epoxy puck and polished (see Fig. 4-F).

Five samples were analyzed by U-Pb geochronology on apatite (PY36, PY44-46, PY71, PY72 and PY73 see location Fig. 2-A and GPS in supplementary data 1). The U/Pb apatite geochronology was conducted at the GeOHeLiS analytical platform (Géosciences Rennes laboratory, France). Nine to thirty-nine minerals were analyzed depending on the sample, by in-situ laser ablation inductively coupled plasma-mass spectrometry (LA-ICP-MS) using a ESI NWR193UC Excimer laser coupled to a quadripole Agilent 7700x ICP-MS equipped with a dual pumping to enhance sensitivity (Paquette et al., 2014). For more instrumental setting details see Pochon et al. (2016) and supplementary data 2. During ablation, 50 μm-wide ablation spots were performed. The data obtained were corrected for mass bias and U-Pb fractionation by standard bracketing with repeated measurements of the Madagascar apatite standard (Thomson et al., 2012), while the Durango (31.44 ± 0.18 Ma; (McDowell et al., 2005)) and McClure (523.51 ± 2.09 Ma;

Table 1
Apatite U–Pb data obtained by in situ laser ablation ICP-MS.

Sample	U (ppm)	Pb (ppm)	$^{238}U/^{206}Pb$	Error (2σ)	$^{207}Pb/^{206}Pb$	Error (2σ)	Final ^{207}Age	Error (2σ)
PY36 andesitic dyke (Forced intercept at 0.990–1853 ± 44 Ma U-Pb ap)								
ApatBatch25a_14	1.1	3.9	1.314	8.9	0.6100	3.1	1843	230
ApatBatch25a_15	1.0	2.9	1.432	7.2	0.5690	3.0	1901	220
ApatBatch25a_16	1.9	7.0	1.288	6.0	0.6100	1.5	1890	290
ApatBatch25a_18	1.1	3.2	1.428	6.4	0.5770	2.6	1874	280
ApatBatch25a_23	1.7	5.2	1.808	6.2	0.4570	2.8	1884	160
ApatBatch25a_24	0.9	3.5	1.179	9.0	0.6330	3.5	1890	270
ApatBatch25a_26	1.5	4.8	1.551	5.5	0.5470	1.8	1831	200
ApatBatch25a_27	0.8	3.0	1.264	5.9	0.6080	2.5	1891	190
ApatBatch25a_28	0.8	2.9	1.318	5.5	0.6240	2.2	1846	270
ApatBatch25a_29	1.2	3.6	1.593	5.7	0.5170	2.3	1905	230
ApatBatch25a_32	0.9	2.7	1.413	6.2	0.5790	2.4	1858	220
ApatBatch25a_33	1.0	4.7	0.988	5.9	0.7010	2.4	1860	340
PY44-46 andesitic dyke (Forced intercept at 0.990–1868 ± 18 Ma U-Pb ap)								
Apat250618b_1	3.3	4.2	2.193	4.4	0.3735	1.7	1799	110
Apat250618b_2	3.0	4.2	2.082	4.5	0.4025	2.1	1811	110
Apat250618b_3	2.9	4.9	1.826	4.7	0.4518	2.0	1894	110
Apat250618b_4	2.7	4.0	1.969	4.7	0.4212	1.9	1851	110
Apat250618b_5	2.7	3.6	2.113	4.6	0.3860	2.6	1827	120
Apat250618b_6	3.1	4.2	2.05	4.5	0.4036	1.9	1826	130
Apat250618b_7	2.2	4.4	1.661	4.6	0.4910	2.2	1922	130
Apat250618b_8	3.4	5.1	2.008	4.6	0.4070	2.0	1864	120
Apat250618b_9	2.5	3.6	2.022	4.4	0.3948	2.2	1886	130
Apat250618b_10	2.4	4.0	1.843	4.6	0.4540	2.2	1862	150
Apat250618b_11	2.1	5.5	1.389	4.9	0.5930	2.0	1840	130
Apat250618b_12	2.5	4.2	1.801	4.3	0.4487	1.7	1928	140
Apat250618b_13	2.1	4.0	1.672	4.3	0.4913	1.8	1926	150
Apat250618b_14	1.8	4.4	1.503	4.8	0.5640	2.7	1811	140
Apat250618b_15	2.7	3.9	2.017	4.4	0.4008	2.0	1872	130
Apat250618b_16	2.6	4.0	1.905	4.4	0.4165	2.1	1934	130
Apat250618b_17	2.8	3.9	2.027	4.4	0.3767	1.9	1934	120
Apat250618b_18	4.0	4.9	2.297	4.3	0.3339	2.8	1827	120
Apat250618b_20	2.8	3.9	1.965	4.4	0.4150	2.9	1879	110
Apat250618b_21	2.6	3.9	1.894	4.3	0.4270	2.0	1919	140
Apat250618b_22	1.7	5.0	1.248	4.4	0.6190	1.8	1924	190
Apat250618b_23	2.8	4.3	1.88	4.5	0.4347	1.8	1876	120
Apat250618b_24	2.6	4.2	1.908	4.9	0.4352	2.3	1874	130
Apat250618b_25	3.1	4.2	2.056	4.3	0.3888	2.1	1869	110
Apat250618b_26	2.7	6.1	1.519	4.4	0.5421	1.7	1889	130
Apat250618b_27	3.6	4.5	2.195	4.3	0.3490	1.9	1875	100
Apat250618b_29	2.9	4.2	2.04	5.3	0.4020	2.7	1845	110
Apat250618b_30	2.9	3.9	2.071	4.5	0.3790	1.9	1898	110
Apat250618b_32	2.8	3.7	2.04	4.5	0.3820	2.6	1896	110
Apat250618b_33	2.8	4.0	1.964	4.3	0.3937	1.8	1945	120
Apat250618b_34	3.1	4.2	2.029	4.4	0.3743	2.0	1958	120
Apat250618c_1	2.9	4.1	1.917	4.6	0.3915	1.9	1990	150
Apat250618c_2	3.3	4.4	2.051	4.7	0.3711	1.7	1932	130
Apat250618c_4	3.2	4.3	2.06	5.1	0.3690	2.5	1941	130
Apat250618c_5	2.6	3.8	1.954	4.7	0.4073	1.9	1896	130
Apat250618c_6	3.0	4.0	2.052	4.9	0.3728	2.2	1925	120
Apat250618c_10	3.6	4.7	2.197	4.6	0.3587	1.9	1847	130
Apat250618c_11	2.8	4.2	1.98	5.1	0.4130	2.9	1865	140
Apat250618c_12	2.8	4.4	1.937	5.0	0.4361	2.3	1833	140
PY71 basaltic dyke (Forced intercept at 0.990–1898 ± 39 Ma U-Pb ap)								
Apat260618a_1	3.0	4.3	2.074	5.8	0.3721	1.9	1900	170
Apat260618a_2	3.3	4.8	2.059	6.4	0.3930	2.8	1855	170
Apat260618a_3	2.5	4.4	1.809	6.8	0.4600	3.9	1872	190
Apat260618a_4	1.0	1.1	2.129	6.1	0.3130	3.5	2058	180
Apat260618a_5	1.3	2.1	1.747	6.7	0.4420	3.6	2020	240
Apat260618a_6	3.1	4.5	2.005	6.2	0.4030	3.0	1880	170
Apat260618a_7	3.6	4.8	2.127	6.5	0.3690	3.5	1873	190
Apat260618a_9	2.4	3.7	1.849	5.9	0.4292	2.0	1938	160
Apat260618a_10	3.3	4.3	2.042	5.9	0.3832	1.9	1900	170
Apat260618a_11	3.2	4.2	2.079	6.0	0.3837	2.4	1871	170
PY72 basaltic dyke (Forced intercept at 0.990–1890 ± 34 Ma U-Pb ap)								
Apat260618a_14	2.9	4.3	1.939	6.5	0.4090	3.7	1913	170
Apat260618a_16	8.3	11.1	2.679	5.6	0.1716	1.6	1944	130
Apat260618a_17	7.5	9.6	2.833	5.9	0.1726	2.8	1831	120
Apat260618a_18	6.7	9.5	2.706	5.7	0.1790	1.8	1910	130
Apat260618a_19	6.5	8.1	2.76	5.8	0.1728	2.9	1883	140
Apat260618a_20	7.1	9.2	2.746	5.7	0.1709	1.9	1905	130
Apat260618a_21	6.8	9.8	2.564	5.9	0.2085	4.1	1941	110
Apat260618a_22	5.7	7.4	2.642	5.8	0.1813	2.2	1953	140

(*continued on next page*)

Table 1 (*continued*)

Sample	U (ppm)	Pb (ppm)	$^{238}U/^{206}Pb$	Error (2σ)	$^{207}Pb/^{206}Pb$	Error (2σ)	Final ^{207}Age	Error (2σ)
Apat260618a_23	7.1	9.6	2.763	6.1	0.1900	2.5	1847	130
Apat260618a_24	10.0	13.9	2.85	6.0	0.1687	2.1	1839	120
PY73 microgranitic Velho Guilherme dyke (Forced intercept at 0.990–1885 ± 30 Ma)								
Apat250618c_13	7.6	10.8	2.168	5.1	0.3470	2.7	1882	70
Apat250618c_14	6.2	8.1	2.216	5.1	0.3565	2.2	1828	120
Apat250618c_15	11.3	23.4	2.317	4.6	0.3058	1.6	1880	92
Apat250618c_16	15.5	32.3	2.484	4.5	0.2723	1.7	1838	92
Apat250618c_18	14.4	30.7	2.443	4.6	0.2484	2.1	1857	86
Apat250618c_19	7.3	9.4	2.317	4.4	0.2799	1.5	1859	110
Apat250618c_20	7.2	12.8	2.26	4.5	0.3045	1.8	1823	110
Apat250618c_21	6.8	9.3	2.292	7.1	0.2830	3.9	1877	55
Apat250618c_25	6.8	8.9	2.306	4.6	0.3290	1.6	1831	110

(Schoene and Bowring, 2006)) apatite standards were analyzed in the same conditions to control the precision and accuracy of the analyses. Data reduction was carried out with the Iolite software (Paton et al., 2011) and the data reduction scheme VizualAge_UcomPbine (Chew et al., 2014). During the analyses, the McClure and Durango apatite standards yielded ^{207}Pb corrected ages of 526.0 ± 6.6 Ma (MSWD = 1.06; probability = 0.39) and 32.3 ± 0.56 Ma (MSWD = 0.38; probability = 0.997) respectively, see Supplementary data 2.

In two samples (PY44-46 and PY73), some zircons were handpicked. These samples were selected for U-Pb geochronology on zircon. These analyses were carried out by LA-SF-ICP-MS at the Isotopic Geology Laboratory of the Geosciences Institute – UNICAMP (Brazil). Isotope data were acquired using a Thermo Element-XR mass spectrometer coupled to an Excite 193 laser ablation system (Photon Machines). The acquisition protocol includes a spot size of 25 μm with a 10 Hz laser frequency and a 40 s ablation time according the procedures of Navarro et al. (2015). The reference material 91,500 zircon was used as primary standard (Wiedenbeck et al., 1995), and data reduction was performed using Iolite software (Paton et al., 2011). During the course of analyses, the Peixe zircon (age ID-TIMS of 564 ± 4 Ma; (Dickinson and Gehrels, 2003)) was used as a secondary reference mineral and gives an age of 568.6 ± 3.6 Ma (MSWD = 1.4) during our analyses (see supplementary data 3).

3.3. Paleomagnetism

Preparation and analysis of samples were performed in the Paleomagnetic Laboratory of the Instituto de Astronomia e Geofisica of the University of São Paulo (USPMag, Brazil), where cylindrical cores and blocks were prepared in 2.2 cm high standards specimens (1223 in total). In order to isolate a characteristic remanent magnetization (ChRM), conventional stepwise Alternating Field (AF) and thermal demagnetization were performed in a magnetically shielded room with ambient field < 1000 nT. A pre-treatment with low temperature demagnetization (LTD- 5 N_2 baths) was applied on selected specimens to reduce the multidomain (MD) influence before AF and thermal procedures (Borradaile, 1994; Borradaile et al., 2004; Dunlop and Argyle, 1991; Warnock et al., 2000). AF demagnetization was done using a tumbler Molspin AF demagnetizer with steps of 2.5 mT (up to 15 mT) and 5 mT (15–100 mT) and a JR-6A spinner magnetometer (AGICO, Czech Republic) was used to measure the remanence. We also used an automated three-axis AF demagnetizer coupled to a horizontal 2G-Enterprises^{TM} DC-SQUID magnetometer, and an AF demagnetization coils coupled to a vertical 2G-Enterprises^{TM} DC-SQUID magnetometer with an automatic sample changer (Kirschvink et al., 2008). Stepwise thermal demagnetization of 50 °C (until 500 °C) and 20 °C (until 700 °C) were carried out using a TD-48 furnace device. Principal component analysis (PCA) (Kirschvink, 1980) or intersecting great circle technique (Halls, 1978) was used to determine the remanence directions using orthogonal vectors diagrams (Zijderveld, 1967) and/or stereographic projections. Only vectors with mean angular deviation (MAD) smaller than 8° was considered. Mean remanence directions and paleomagnetic poles were calculated using Fisher (1953) statistics. Paleomagnetic data processing and calculations was carried out using PALEOMAC package (Cogné, 2003). GPlates were used for paleogeographic reconstructions (Boyden et al., 2011). In addition, magnetic mineralogy of each site was investigated to determine the carriers of magnetic remanence. Hysteresis loops, isothermal remanent magnetization (IRM) and first order reverse curves (FORC) for selected samples were performed to determine magnetic carriers and domain states, using a MicroMag-VSM, Model 3900 (Princeton Measurements Corporation). Thermomagnetic experiments (susceptibility versus temperature) were conducted in an argon atmosphere in low- and high-temperature conditions using a CS-4 apparatus coupled to the KLY-4S Kappabridge instrument (AGICO, Brno, Czech. Republic). Thin and polished sections were analyzed under transmitted and reflected light microscopy. In addition, Scanning Electron Microscopy (SEM) analysis using a Jeol JSM-6360LV instrument (Géosciences Environnement Toulouse, France) was used to constrain the nature and textures associated with the magnetic carriers.

4. U/Pb geochronological results

4.1. Apatite dating

All the apatite isotopic ratios data are reported in Table 1 and are plotted in Tera-Wasserburg diagrams (Fig. 4) realized using Isoplot/Ex (Ludwig, 2009). All errors are listed at 2 sigmas. For the calculation of the ^{207}Pb corrected ages (Table 1), the initial common $^{207}Pb/^{206}Pb$ value of 0.990 was calculated following the terrestrial Pb evolution model of Stacey and Kramers (1975).

The isotopic data obtained for the PY73 sample (microgranitic dyke) display variable proportions of common Pb with $^{207}Pb/^{206}Pb$ values varying between 0.17 and 0.35. The unforced lower intercept date for this sample is 2007 ± 140 Ma with a MSWD of 1.09. If the Discordia is forced to a $^{207}Pb/^{206}Pb$ value of 0.990 (Fig. 4-A), the resulting lower intercept date is 1885 ± 30 Ma (MSWD = 1.4). The weighted average ^{207}Pb-corrected date is equivalent to the intercept age with a date of 1861 ± 28 Ma (MSWD = 0.28) (see Fig. 4-A).

Data obtained for samples PY36 and PY4446 (andesitic dykes) display variable proportions of common Pb ($^{207}Pb/^{206}Pb$ values between 0.52 and 0.70 and 0.33–0.62, respectively). The data for the PY36 sample define an unforced lower intercept date of 1861 ± 140 with a MSWD of 0.48. If the Discordia is forced to a $^{207}Pb/^{206}Pb$ value of 0.990 (Fig. 4-B), the resulting lower intercept date is equivalent within error at 1853 ± 44 Ma. For sample PY44-46, the unforced lower intercept date is 1873 ± 41 with a MSWD of 1.00. If the Discordia is forced to a $^{207}Pb/^{206}Pb$ value of 0.990 (Fig. 4-C), the resulting lower intercept date is equivalent within error at 1868 ± 18 Ma. The weighted average ^{207}Pb-corrected dates are equivalents, within the error, to 1874 ± 64 Ma (MSWD = 0.05, PY36) and 1882 ± 20 Ma (MSWD = 0.52, PY44-46) (see Fig. 4-B and 4-C).

Data obtained for the samples PY71 and PY72 (basaltic dykes)

Table 2
Zircon U-Pb data obtained by LA-ICP-MS.

Sample	i206 (%)	U (mg.g^{-1})	2 s	Th (mg.g^{-1})	2 s	Pb (mg.g^{-1})	2 s	Th/U	Measured ratios								Ages (Ma)							
									$^{206}Pb/^{204}Pb$	$^{207}Pb/^{235}U$	1s	1s %	$^{206}Pb/^{238}U$	1s	1s %	Rho	$^{207}Pb/^{206}Pb$	2s	$^{206}Pb/^{238}U$	2s	$^{207}Pb/^{235}U$	2 s	% conc^{2}	
Microgranitic Velho Guilherme dyke																								
ELD73_4	0.14	70	2	52	1	55	2	0.74	13,060	5.640	0.110	2.0	0.3433	0.0066	1.9	0.49	1922	21	1892	31	1914	16	98	
ELD73_7	0.15	70	3	66	2	69	3	0.95	12,420	5.590	0.100	1.8	0.3473	0.0070	2.0	0.48	1885	22	1919	33	1915	15	102	
ELD73_11	0.11	98	4	90	4	92	5	0.92	16,650	5.509	0.093	1.7	0.3388	0.0063	1.9	0.49	1901	19	1876	30	1898	15	99	
ELD73_13	0.14	79	3	76	2	79	4	0.96	13,210	5.520	0.130	2.4	0.3448	0.0086	2.5	0.37	1922	28	1904	41	1902	19	99	
ELD73_15	0.09	129	8	120	7	115	8	0.93	21,450	5.470	0.100	1.8	0.3409	0.0066	1.9	0.47	1905	20	1888	32	1896	16	99	
ELD73_17	0.08	146	7	130	7	123	7	0.89	24,200	5.412	0.096	1.8	0.3401	0.0066	1.9	0.53	1921	18	1880	32	1882	15	98	
Andesitic dyke																								
ELD46_2	0.05	191	12	92	6	82	5	0.48	39,450	5.783	0.090	1.6	0.3727	0.0061	1.6	0.52	1883	15	2038	29	1938	13	108	
ELD46_3	0.25	38	1	33	2	35	2	0.86	7385	5.630	0.130	2.3	0.3463	0.0080	2.3	0.50	1931	24	1912	38	1909	20	99	
ELD46_4	0.17	57	3	70	4	67	4	1.23	11,200	5.460	0.120	2.2	0.3356	0.0075	2.2	0.38	1941	26	1861	36	1883	19	96	
ELD46_5	0.08	116	5	145	5	144	6	1.25	23,450	5.530	0.100	1.8	0.3448	0.0068	2.0	0.51	1899	20	1905	32	1906	16	100	
ELD46_6	0.27	37	2	35	1	38	2	0.95	7025	5.650	0.140	2.5	0.3475	0.0079	2.3	0.39	1958	26	1918	37	1919	21	98	

display variable proportions of common Pb as indicated by their $^{207}Pb/^{206}Pb$ values between 0.31 and 0.46 and 0.17–0.41, respectively. For sample PY71, the data yield an unforced lower intercept date of 1949 ± 190 (MSWD = 1.06) within error similar to the date of 1898 ± 39 Ma (MSWD = 0.97) obtained when the $^{207}Pb/^{206}Pb$ value is forced to 0.990 (Fig. 4-D). For sample PY72, the lower unforced intercept yields a date of 1885 ± 48 Ma (MSWD = 0.69). If the Discordia is forced to a $^{207}Pb/^{206}Pb$ value of 0.990, we obtain a similar date of 1890 ± 34 Ma (MSWD = 0.62). The weighted average ^{207}Pb-corrected dates are equivalents, within the error, for both samples at 1912 ± 55 Ma (MSWD = 0.53, PY71) and 1895 ± 40 Ma (MSWD = 0.52, PY72) (see Fig. 4-D and 4-E).

4.2. Zircon dating

For the microgranitic dyke PY73, 6 zircon spots yield a Concordia age of 1903 ± 13 Ma (2σ, MSWD = 0.28) (Table 2; Fig. 5-A). The weighted mean age $^{207}Pb/^{206}Pb$ of 1909 ± 8.5 (MSWD = 2) is equivalent within error limits. The andesitic dyke PY44-46 show a Concordia age of 1909 ± 19 Ma (MSWD = 1.14) (Table 2; Fig. 5-B). This age is equivalent within error limits to an upper intercept age of 1911 ± 21 Ma (MSWD = 0.24) and a weighted mean age $^{207}Pb/^{206}Pb$ of 1927 ± 42 Ma (MSWD = 4.9).

5. Paleomagnetic results

5.1. Magnetic components

Paleomagnetic results of the Tucumã and Rio Maria dyke swarms record a complex history where primary component is partially or wholly overprinted by secondary natural remanent magnetizations (NRMs). To resolve and isolate the magnetic components AF treatment was generally more efficient than thermal demagnetization which reveal for some samples a characteristic "tail", typical feature of multidomain (MD) grains (Dunlop and Özdemir, 2000; Shcherbakova et al., 2000) (Fig. 6-A). After removal of randomly oriented secondary components, most of sites reveal a stable characteristic remanent magnetization (ChRM) with a steep inclination for these Carajás Dykes (CD1 component). Samples of the ~1880 Ma andesitic (PY36C2, Fig. 6-A) and basaltic (PY72A1, Fig. 6-B) dykes show a north/northeastern, steep upward inclination direction with unblocking temperature ranging between 300 and 580 °C and high coercivities (>25mT). Occurrence of reverse polarity appears in the ~1880 Ma microgranitic dykes (Fig. 6-C, E) and some basaltic dykes (Fig. 6-D). No stable components with unblocking temperatures higher than 600 °C were found in these samples, even in those from microgranitic dykes.

A second southwestern (northeastern), low inclination direction (component CD2) was revealed in some microgranitic dykes and even in the granodioritic host rocks (~2870 Ma) cropping out in the studied area. This component was observed in the microgranitic dyke of the Velho Guilherme suite (~1855 Ma) after LTD treatment (~60% of remanence was removed) followed by thermal demagnetization, and associated with unblocking temperatures between 400 °C and 600 °C (Fig. 6-F).

A third northern, low upward inclination component (CD3) was isolated for younger basaltic dykes, after removing secondary directions with coercivities lower than 12 mT (Fig. 6-G). One of these NS gabbroic dykes cuts Paleoproterozoic dykes and a baked contact test was performed for it (see below). Similar directions were also observed on nine Paleoproterozoic dykes and Archean basement rocks as secondary components.

A fourth component (CD4) is characterized by northern, low downward inclination directions (Fig. 6-H) and was found in 11 collected basaltic dykes. On fresh basaltic dykes this component is carried by magnetite with high unblocking temperatures (520–580 °C) suggesting a primary character for it. Some ~1880 Ma microgranitic dykes showed

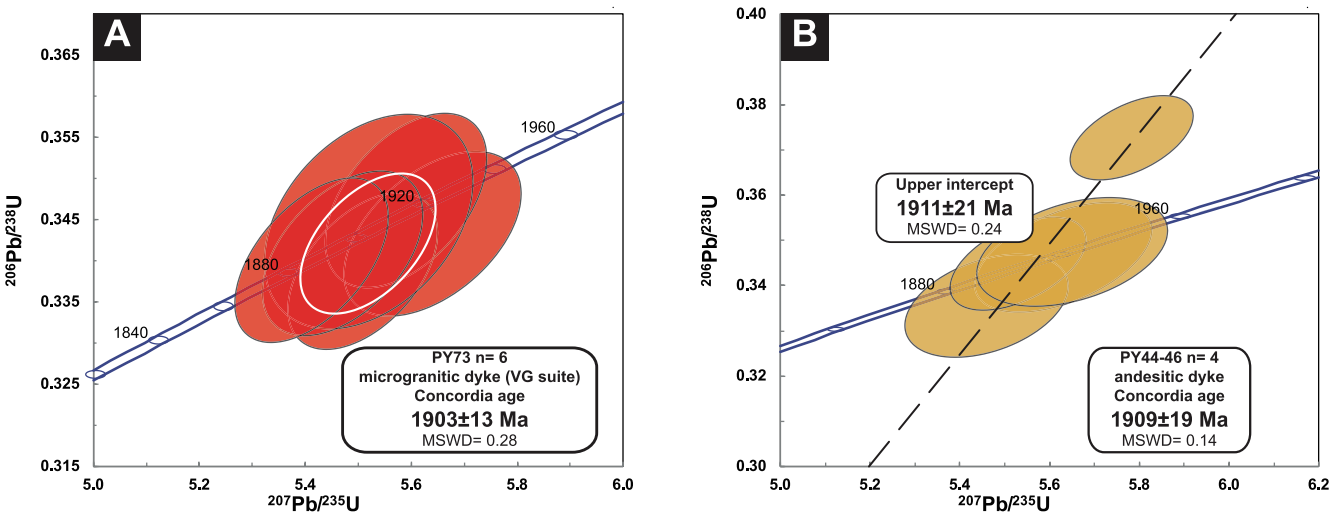

Fig. 5. U-Pb concordia diagram of zircon analyses from the PY73 microgranitic dyke (A) and from the PY44-46 andesitic dyke (B).

also the same component and should represent a younger remagnetization.

5.2. Site mean directions and paleomagnetic poles

Normal (6 dykes) and reverse (10 dykes) polarities were found for the CD1 component. This stable component was isolated for microgranitic, andesitic and basaltic dykes well-dated at ~1880 Ma in this study. A mean direction was calculated for the CD1 component using both normal and reverse site mean directions: Dm = 125.9°, Im = 73.8° (α_{95} = 5.9°, k = 40.4), and the respective CD1 paleomagnetic pole is located at 334.3°E, 23°S (A_{95} = 9.8° K = 15.2) (Table 3; Fig. 7-A). CD1 component is similar to the SF1 component calculated for the volcanic rocks of the ~1880 Ma Santa Rosa Formation, located ~300 km to the west of Tucumã, and interpreted as a primary magnetization acquired during rock intrusion (Antonio et al., 2017). The SF1 component obtained in the rhyolitic rocks of São Felix do Xingu is carried by hematite with high unblocking temperatures (620 °C–700 °C) (Antonio et al., 2017). The SF1 and CD1 components exhibited both polarities.

In view of the similarity in the directions of both SF1 and CD1 components (Fig. 7-B), we can use this dataset to calculate a grand mean pole for the Uatumã SLIP, *i.e.*, a mean pole calculated from multiple distinct but broadly coeval cooling units of a large igneous province (*e.g.*, the Umkondo LIP; (Swanson-Hysell et al., 2015)). The grand mean direction (named CA1 - Carajás component) was calculated for the Carajás magmatic event: Dm = 132.8°, Im = 76° (N = 26, α_{95} = 5°, k = 32.7). The respective CA1 paleomagnetic pole is located at 328.7°E, 23.3°S (A_{95} = 8.7° K = 11.7) (Table 4; Fig. 7-B). Nine among the twenty-six sites of the CA1 pole were precisely dated by U-Pb method (zircon and baddeleyite) (Antonio et al., 2017; Oliveira, 2006; Pinho et al., 2006; Silva et al., 2016; Teixeira et al., 2019b), Pb-Pb evaporation on zircon (Oliveira, 2006; Pinho et al., 2006) and U-Pb on apatite at 1880 Ma (Table 2; Fig. 4). CA1 grand mean pole pass the reversal test (McFadden and McElhinny, 1990). The critical gamma of 10.6° is greater than the angle between the normal and reversed axes (1.9°), and the test is classified as "C". So, it can be considered as positive using the 26 sites.

The CD2 component observed in 6 sites in the Tucumã-Rio Maria area is composed of magnetic directions with both polarities. The CD2 site mean directions cluster around the mean: Dm = 239.3°, Im = 19.6° (N = 6, α_{95} = 21.4°, k = 10.7) and the CD2 paleomagnetic pole is located at 227°E, 30.4°S (A_{95} = 18.4° K = 14.6) (Table 3; Fig. 7-C). This CD2 component is also carried by three sites of the Archean rocks sampled far from each other, and not close to the contact of any dyke. This could imply a regional remagnetization. However, the CD2 component is similar to the SF2 component of the São Felix do Xingu volcanic rocks, for which a positive baked contact test attests to the primary nature of the SF2 magnetization acquired at ~1855 Ma (Antonio et al., 2017). Therefore, a combined mean including both CD2 and SF2 site mean directions was calculated and named as the CA2 component: Dm = 240.3°, Im = 11.8° (N = 18, α_{95} = 10.8°, k = 11.1), with a corresponding paleomagnetic pole located at 221.3°E, 30.2°S (A_{95} = 8.8° K = 16.2) (Table 4; Fig. 7-D). The means of reverse and normal polarity site mean directions form a similar cluster with k1 = k2 at 99% of confidence according to McElhinny (1964) and similar directions with a difference of 10.0° in declination (Table 4), but the reversal test is undetermined (McFadden and McElhinny, 1990).

The CD3 component was firstly calculated only for the basaltic dykes where field evidence suggests they are Mesozoic (at baked contact tests or cross-cutting older dykes). For these dykes, the site mean directions group around Dm = 357.3°, Im = −25.7° (N = 8, α_{95} = 11.9°, k = 22.7), which yielded the paleomagnetic pole located at 352.6°E, 82.3°S (A_{95} = 9.5° K = 35) (Table 3; Fig. 8-A). Only one polarity was found on these dykes. The CD3 component was also disclosed for some ~1880 Ma microgranitic dykes and even for host rocks close to these basaltic dykes suggesting a regional remagnetization during this magmatic event (Fig. 8-B). These site mean directions cluster around the mean Dm = 351.4°, Im = −24.6° (N = 9, α_{95} = 17.7°, k = 9.0). This mean direction is close to the CD3 component calculated for the Mesozoic dykes (see above).

The CD4 component is characterized by remanent magnetizations northerly directed and with low downward inclinations. Their site mean directions group around Dm = 352.7°, Im = 33.3° (N = 11, α_{95} = 10.7°, k = 19) and the CD4 paleomagnetic pole is located at 113.7°E, 63.4°S (A_{95} = 10.8° K = 18.7) (Table 3; Fig. 8-C). This magnetic component was disclosed for basaltic dykes, whose magnetic carriers are characterized by high unblocking temperatures, suggesting a primary origin, but it was also found on ~1880 Ma microgranitic dykes. Unfortunately, no radiometric age on these basaltic dykes is presently available to determine the age of the CD4 component.

6. Baked contact test

Fig. 9-A is a schematic sketch showing a younger NS gabbroic dyke cross-cutting a NW microgranitic dyke in the Tucumã area. Despite the difficulty to find blocks in situ, it was possible to perform a reverse baked contact test between a small ramification of this younger NS gabbroic dyke and the ~1880 Ma microgranitic dyke where the contact was

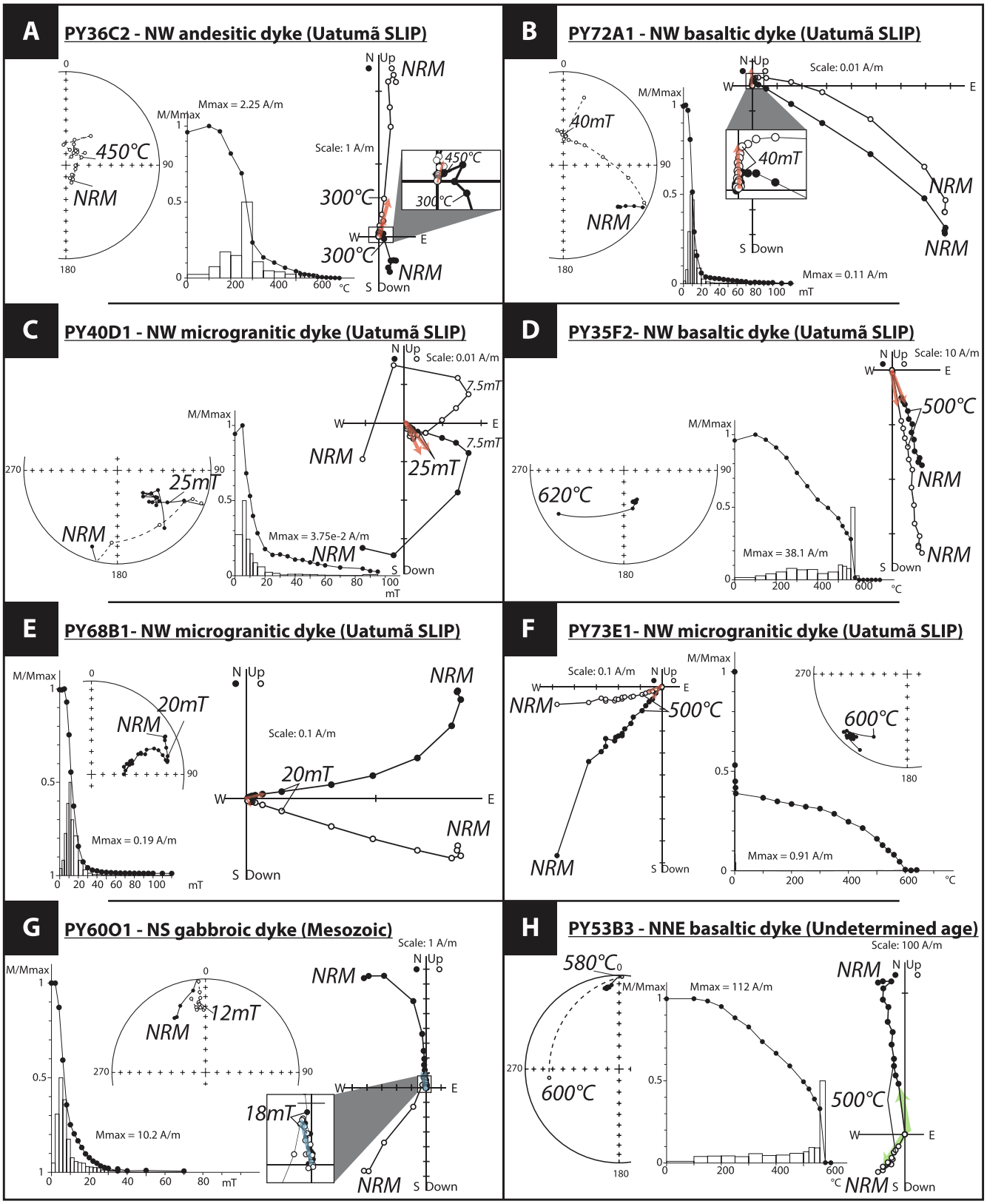

Fig. 6. Examples of AF (alternating field) and thermal demagnetization for Andesitic (A-B), basaltic (C-D) and microgranitic (E-F) dykes from the Carajás dyke swarm. G and H are examples for younger dykes in the area. Demagnetization results are presented with stereographic projections, orthogonal projections (Zijderveld plot) and normalized magnetization intensity curves.

Table 3

Results of paleomagnetic data. n/N – number of analyzed samples/number of samples used in the mean; Dec (°) – declination; Inc (°) – inclination; α_{95}, r is the resultant vector, k – Fisher's confidence cone and precision parameter (Fisher, 1953); *G.C* –Great circles analysis. VGP – Virtual Geomagnetic Pole; P. Long – Paleolongitude; P. Lat – Paleolatitude. Values in bold are for the mean directions (N, Dec, Inc, R, K and A_{95} – P. Lat, P. Long). *: Sites discarded with $\alpha_{95} > 20°$ or not in situ (PY25-26).

Site	Sample	Lithology	S.Lat	S.Long	Characteristic remanent magnetization (ChRM)						VGP	
					n/N	Dec (°)	Inc (°)	R	k	α95 (°)	P. Lat (°N)	P. Long (°E)
CD1												
Normal polarity												
12*	PY25-26	*NW - Microgranitic dyke*	-7.45	-49.87	8/11	92.2	-67.5	7.78	32.5	9.9	-3.8	271.1
17*	PY31	*NW- Andesitic dyke*	-7.4	-50.14	7/7	298.6	-38.5	6.66	17.4	15	-28	16.7
18	PY32-33-34	*NW- Andesitic dyke*	-7.4	-50.14	9/12	297.4	-68.4	8.72	28.8	10.5	-22.6	346.6
20	PY36-37-38	*NW- Andesitic dyke*	-7.4	-50.14	8/15	232.5	-83.7	7.84	42.9	8.6	0.3	319.8
13	PY27 $_{A-E}$	*NW - Basaltic dyke*	-7.44	-50.02	6/9	295.6	-58.1	5.73	18.6	16.5	-24.5	0.6
14	PY28 $_{F-L}$	*Archean basement*	-7.43	-50.03	6/10	268.3	-81.6	5.88	42	11.7	-6.6	326.6
17*	PY31 $_{A-C\ -\ H}$	*Archean basement*	-7.4	-50.14	3/5	289.1	-29.8	2.9	20.8	27.8	-20.3	25.5
45	PY67 A-G	*NW - Microgranitic dyke*	-6.8	308.66	7/12	342.7	-81.4	6.8	29.5	11.9	22.8	134.1
50	PY72 A-F	*NW - Basaltic dyke*	-6.82	308.6	12/14	1.6	-60.2	11.9	106	4.3	55.6	126.5
MEAN CD1 (N)					***6***	***312.2***	***-75.6***	***5.8***	***24.9***	***13.7***		
								R=5.47	***K=9.5***	***A95=22.9***	***22.8***	***150.1***
Reversed polarity												
22	PY40	*NW - Microgranitic dyke*	-7.41	-50.21	6/8	115.7	67.8	*5.9*	*52.2*	11.1	-21.8	347.7
24	PY44-45-46	*NW- Andesitic dyke*	-7.52	-50.05	8/19	170.1	76.5	7.7	23	11.8	-32.7	315
15*	PY29 $_{A-G}$	*NW - Basaltic dyke*	-7.52	-50.02	4/10	71.7	55.3	3.63	8.1	34.4	10.1	1.4
16	PY30 $_{A-D/I-L}$	*NW - Basaltic dyke*	-7.76	-50.05	9/12	105.4	68.1	8.88	66.4	6.9	-15.7	348.8
19	PY35 $_{A-H}$	*NW - Basaltic dyke*	-7.38	-50.13	6/12	126	63.8	5.88	40.8	10.8	-30	350.9
21*	PY39	*NW- Andesitic dyke*	-7.38	-50.13	6/8	235.9	**57.3**	5.95	108.6	7.7	-31.2	260.1
22*	PY40 $_{F-G}$ - PY41-42	*Archean basement*	-7.41	-50.21	4/5	107.4	81.6	3.76	12.3	28.8	-12	325.8
40	PY62 J-Q	*NW - Microgranitic dyke*	-6.76	308.56	10/24	111.8	60.3	9.93	122.4	4.6	-20.8	356.9
46	PY68 A-F	*NW - Microgranitic dyke*	-6.8	308.66	9/12	162.2	85.9	8.81	42	8.3	-14.6	311.3
48	PY70 A-G	*NW - Microgranitic dyke*	-6.8	308.66	10/13	126.1	78.8	10.77	G.C	13.8	-19	327
52	PY74 A-G	*NW - Microgranitic dyke*	-6.86	308.62	5/11	153.5	80.3	3.39	G.C	14.3	-23.6	317.7
54	PY78 - 79	*NW - Microgranitic dyke*	-6.96	308.75	9/15	142.1	69.7	8.85	54.8	7.3	-34.3	335.1
49	PY71 A-G	*NW - Basaltic dyke*	-6.77	308.66	9/12	97	63.4	8.8	40.5	8.5	-9.7	354.2
MEAN CD1 (R)					***10***	***122.9***	***72.6***	***9.84***	***55.5***	***6.5***		
								R=9.55	***K=20.1***	***A95=11.1***	***-23.1***	***336.7***
MEAN POLE CD1 DYKE (N+R)					***16***	***125.9***	***73.8***	***15.63***	***40.4***	***5.9***		
								R=15.01	***K=15.2***	***A95=9.8***	***-23***	***334.3***
CD2												
Normal polarity												
49	PY71 A-G	*NW - Basaltic dyke*	-6.77	308.66	7/12	*84.1*	*-31.3*	*6.7*	*22.5*	*13*	*7*	*55.3*
54	PY78 - 79	*NW - Microgranitic dyke*	-6.96	308.75	5/15	70.7	-14.7	4.88	34.7	14.1	19.9	44.2
Reversed polarity												
51	PY73 A-H	*NW - Microgranitic dyke*	-6.84	308.58	10/13	224.5	4.7	9.7	30.5	8.9	-45.4	215
16	PY30 $_{E-H}$	*Archean basement*	-7.76	-50.05	7/7	217.7	-4.7	6.54	13.1	17.3	-51	206.4
36	PY58 G-K	*Archean host*	-6.76	308.56	9/11	228.3	24.8	8.76	34	9	-42.1	230
46	PY68 G-K	*Archean host*	-6.8	308.66	7/7	258.2	41.5	6.81	31.7	10.9	-13.5	241.7
MEAN POLE CD2 DYKE (N+R)					***6***	***239.3***	***19.6***	***5.53***	***10.7***	***21.4***		
								R=5.65	***K=14.6***	***A95=18.2***	***-30.4***	***227***
Primary dyke												
14	PY28 $_{A-E}$	*NNE - Basaltic dyke*	-7.43	-50.03	7/11	*352.3*	*-15.4*	*6.87*	*45.4*	*9.5*	*82.4*	*216.2*
25	PY47 $_{A-C}$	*NW - Basaltic dyke*	-7.43	-50.04	4/7	*20.6*	*-48.6*	*3.94*	*52.9*	*14.8*	*60.6*	*91.5*
29	PY51 $_{A-M}$	*NNE - Basaltic dyke*	-6.9	-49.65	8/13	*3.7*	*-2.5*	*7.8*	*35.2*	*10.3*	*83.3*	*343.7*
40	PY62 A-F	*NS - Gabbro dyke*	-6.76	308.56	8/8	357.7	-19.3	7.97	244.9	3.7	86.1	164.4
42	PY64 A-H	*NW - Basaltic dyke*	-6.8	308.63	6/8	339.8	-27.5	5.93	67	9.8	68.7	195.5
44	PY66 A-G	*NW - Basaltic dyke*	-6.8	308.64	4/5	357.9	-22	4.58	G.C	21	-3.4	213.8
38	PY60 I-Q	*NS - Gabbro dyke*	-6.76	308.56	14/15	355.5	-28.6	13.89	112.9	3.9	80.5	155.8
41	PY63 A-G	*NS - Gabbro dyke*	-6.76	308.56	8/8	356.7	-39.3	*7.68*	*21.6*	13.6	74.2	139.9
MEAN POLE CD3 ONLY PRIMARY DYKE					***8***	***357.3***	***-25.7***	***7.7***	***22.7***	***11.9***		
								R=7.8	***K=35***	***A95=9.5***	***82.3***	***145.6***
											-82.3	***325.6***
Remagnetized sites CD3												
32	PY54 $_{A-H}$	*NNE - Basaltic dyke*	-6.92	-50.26	4/4	*356.7*	*-35.9*	*3.88*	*24.9*	*21.7*	*76.6*	*143.2*
27	PY49 $_{A-F}$	*NW - Basaltic dyke*	-6.84	-50.19	5/11	*317.8*	*-1.5*	*5.66*	*14.8*	*18*	*47.5*	*226.1*
38	PY60 A-H	*NW - Basaltic dyke*	-6.76	308.56	6/7	1.8	-30.7	5.92	62.8	10.1	80.1	118.5
36	PY58 A-F	*NW - Microgranitic dyke*	-6.76	308.56	6/14	358.5	-37.4	5.94	97.4	8.1	75.8	134.3
40	PY62 G-F	*NW - Microgranitic dyke*	-6.76	308.56	5/6	20.4	-5	4.9	40.6	12.2	-67.6	194.7
41	PY63 H-J	*NW - Microgranitic dyke*	-6.76	308.56	4/6	351.1	-33.7	1.41	G.C	12.2	75.5	164.4
47	PY69 A-H	*NW - Microgranitic dyke*	-6.81	308.68	6/12	4.2	-30.7	5.95	107.6	6.8	79.4	106.2
14	PY28 $_{F-L}$	*Archean basement*	-7.43	-50.03	3/10	325.4	-4.5	2.95	42.2	19.2	*55.2*	*226.7*
38	PY60 R-Z	*Archean host*	-6.76	308.56	7/9	7.7	-38.2	6.97	219.5	4.4	73.5	102.5
MEAN POLE CD3 REMAGNETIZATION					***9***	***351.4***	***-24.6***	***8.2***	***9.9***	***17.2***		
								R=8.4	***K=13.3***	***A95=14.6***	***79.8***	***179.4***
											-79.8	***359.4***
CD4 - Younger undetermined component (or Neoproterozoic?)												
23	PY43 $_{A-D}$	*NW - Basaltic dyke*	-7.38	-50.13	6/7	*8.6*	*40.9*	*5.89*	*46.5*	*10.6*	*58.1*	*324.9*
26	PY48 $_{A-F}$	*NNE - Basaltic dyke*	-6.86	-50.19	8/9	*12.9*	*25.6*	*7.84*	*43.9*	*8.7*	*65.9*	*342.2*
28	PY50 $_{A-F}$	*NNE - Basaltic dyke*	-6.84	-50.19	8/10	*348.9*	*24.7*	*7.71*	*24.4*	*11.9*	*67.4*	*280.6*

(*continued on next page*)

Table 3 (*continued*)

Site	Sample	Lithology	S.Lat	S.Long	Characteristic remanent magnetization (ChRM)						VGP	
					n/N	Dec (°)	Inc (°)	R	k	α95 (°)	P. Lat (°N)	P. Long (°E)
30	PY52 $_{A-H}$	*NNE - Basaltic dyke*	-6.91	-49.66	8/12	*352.5*	*21.6*	*7.76*	*29.3*	*10.6*	*70.4*	*287.8*
31	PY53 $_{A-H}$	*NW - Basaltic dyke*	-6.91	-50.26	5/5	*352*	*21.7*	*4.9*	*41.8*	*12.8*	*70.2*	*286*
35	PY57 A-D	*NW - Basaltic dyke*	-6.73	308.51	4/6	323.6	50.6	3.99	298.4	5.3	38.5	268.1
33	PY55 A-E	*NW - Microgranitic dyke*	-6.75	308.5	9/12	28.1	43.4	10.63	27.1	9.1	47.8	347.9
34	PY56 A-H	*NW - Microgranitic dyke*	-6.73	308.51	9/15	356.2	42.2	8.9	78.1	6.1	58.7	301.8
37	PY59 A-F	*NW - Microgranitic dyke*	-6.77	308.56	13/14	339.6	13.8	12.83	70.3	5.1	65.4	252.4
39	PY61 A-E	*NW - Microgranitic dyke*	-6.8	308.63	5/10	347.1	34.1	6.94	G.C	10.7	61.5	282.3
41	PY63 K	*NW - Microgranitic dyke*	-6.76	308.56	2/2	331.3	35.2	1.99	647.2	9.8	51.4	262
MEAN POLE CD4					***11***	***352.7***	***33.3***	***10.47***	***19***	***10.7***		
								R=10.47	***K=18.7***	***A95=10.8***	***63.4***	***293.7***
											-63.4	***113.7***

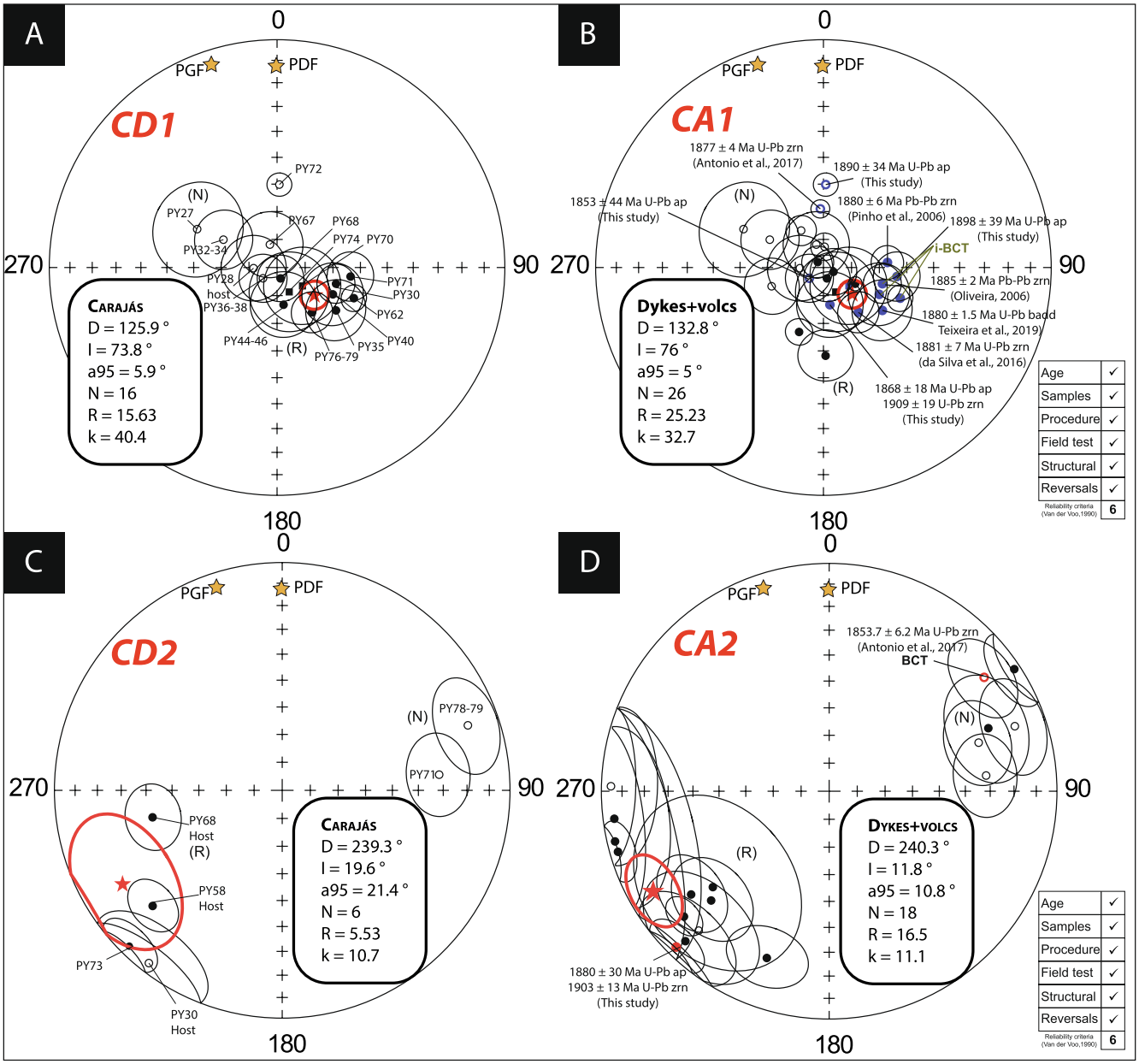

Fig. 7. Stereographic projections of site mean directions (and their confidence circles, α_{95}) for the Carajás Province. A: Site mean directions for the CD1 component of Carajás Dykes, and B: the Grand mean sites CA1 calculated with the combined results of the volcanic units from the São Felix do Xingu area (Antonio et al., 2017). C: represents the site mean directions for the CD2 component for the Carajás dykes, and D: the Grand mean pole CA2 calculated combined with the volcanic units. Red star in each stereogram represents the mean (and its confidence circle, α_{95}) of the site mean directions. PDF – Present Dipolar Field; PGF – Present Geomagnetic Field. (For interpretation of the references to color in this figure legend, the reader is referred to the web version of this article.)

Table 4
Grand mean poles calculated in this study. Combined paleomagnetic pole CA1 using the Carajás dykes (CD1) and associated volcanic rocks of São Felix do Xingu area (SF1) (Antonio et al., 2017). Combined paleomagnetic pole CA2 using the Carajás dykes (CD2) and associated volcanic rocks of São Felix do Xingu area (SF2) (Antonio et al., 2017). N – number of sites (single geographic locality), Dec (°) – declination; Inc (°) – inclination; α_{95}, k – Fisher's confidence cone and precision parameter (Fisher, 1953). Paleomagnetic pole; P. Long – Paleolongitude; P. Lat – Paleolatitude, R is the resultant vector, K is precision parameter, S is the angular dispersion, and A95 is radius of the circle of 95% confidence of the paleomagnetic pole.

Grand mean poles		Site mean directions						Paleomagnetic poles					
Name	Polarity	N	D_m (°)	I_m (°)	R	k	α95 (°)	Lat	Long	K	R	S	A95 (°)
CA1	Normal	10	315.6	−76.9	9.7	29.9	9	23.1	146.7	10.7	9.16	14.9/25	15.5
CA1	Reversed	16	131.2	75.4	15.54	32.4	6.6	−23.4	330	11.6	14.71	14.3/24	11.3
CA1	**Combined**	**26**	**132.8**	**76**	**25.23**	**32.7**	**5**	**−23.3**	**328.7**	**11.7**	**23.87**	**14.2/23.9**	**8.7**
CA2	Normal	6	67.1	−11.4	5.55	11.2	20.9	23	41.8	25.2	5.8	16.1	13.5
CA2	Reversed	12	236.9	12	10.98	10.7	13.9	−34	221	14.1	11.22	21.8	12
CA2	**Combined**	**18**	**240.3**	**11.8**	**16.5**	**11.1**	**10.8**	**−30.2**	**221.3**	**16.2**	**16.95**	**20.3**	**8.8**

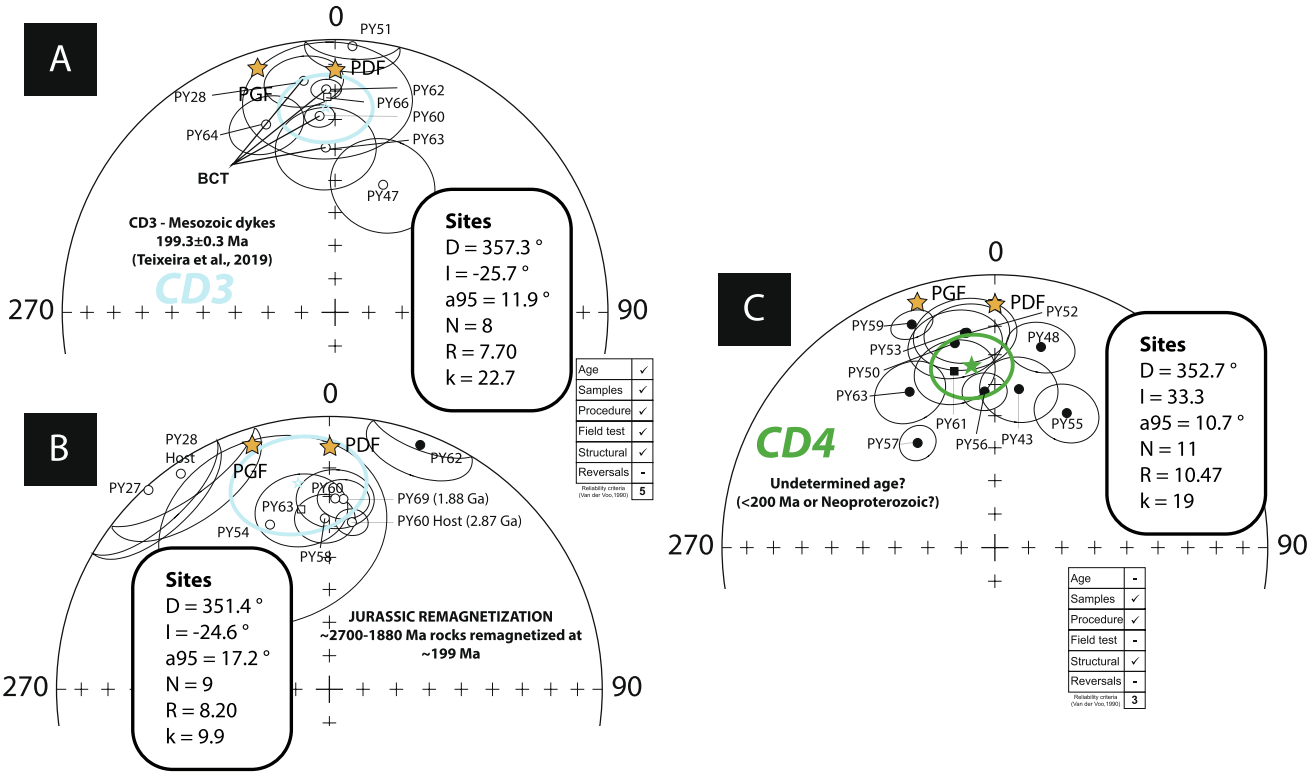

Fig. 8. A: Stereographic projections of site mean directions for the primary Mesozoic dykes (~199 Ma). B: Site mean direction for the Archean/Paleoproterozoic sites re-magnetized during this Jurassic event. C: Site mean directions for the CD4 component (undetermined age). Blue (or red) star in each stereogram represents the mean (and its confidence circle, α_{95}) of the site mean directions. PDF – Present Dipolar Field; PGF – Present Geomagnetic Field. (For interpretation of the references to color in this figure legend, the reader is referred to the web version of this article.)

visible. According to the mean direction, the gabbroic dyke (PY62) is associated to the Jurassic CAMP event (Dm = 357.7°, Im = −19.3°, α_{95} = 3.7°) (Table 3; Fig. 9-B). At contact (<10 cm), the microgranitic samples show a similar direction (Dm = 20.4°, Im = −5°, α_{95} = 12.2°) (Table 3). In contrast, samples collected far away from the contact (>3 m) show a different direction (Dm = 111.8°, Im = 60.3°, α_{95} = 4.6°) (Table 3; Fig. 9-B). This reverse contact test confirms that these microgranitic samples near to the contact were baked during the intrusion of the dyke at ~200 Ma. The different remanent magnetization direction, with unblocking temperatures >450 °C, isolated for samples far away of the dyke contact indicates that this direction is older than 200 Ma. No hybrid direction was found in the collected samples (Fig. 9-B).

FORC experiments were conducted on samples of the gabbroic dyke and for samples of the microgranitic dyke at the contact and far away it (Fig. 9-C). The FORC diagram for a sample from the younger Mesozoic dyke (PY62A1) shows that magnetic mineralogy is controlled by a mixture of MD and mainly PSD magnetite (Roberts et al., 2014). For a sample of the microgranite at the contact (PY62G1, 3 cm), the FORC diagram shows only the PSD magnetite behavior like the younger Mesozoic dyke. This behavior contrasts with that of sample PY62Q1 at 8 m away of the contact where SD behavior prevails, that is, higher coercivities are dominant. This suggests that the younger Mesozoic dyke affected the magnetic mineralogy close to the contact remagnetizing the rock. Modification of the magnetic mineralogy in the host rock according the distance at contact during the dyke's intrusion was already documented (Hyodo and Dunlop, 1993). These results also suggest that FORC diagrams can be a powerful tool to detect magnetic changes within a baked contact test.

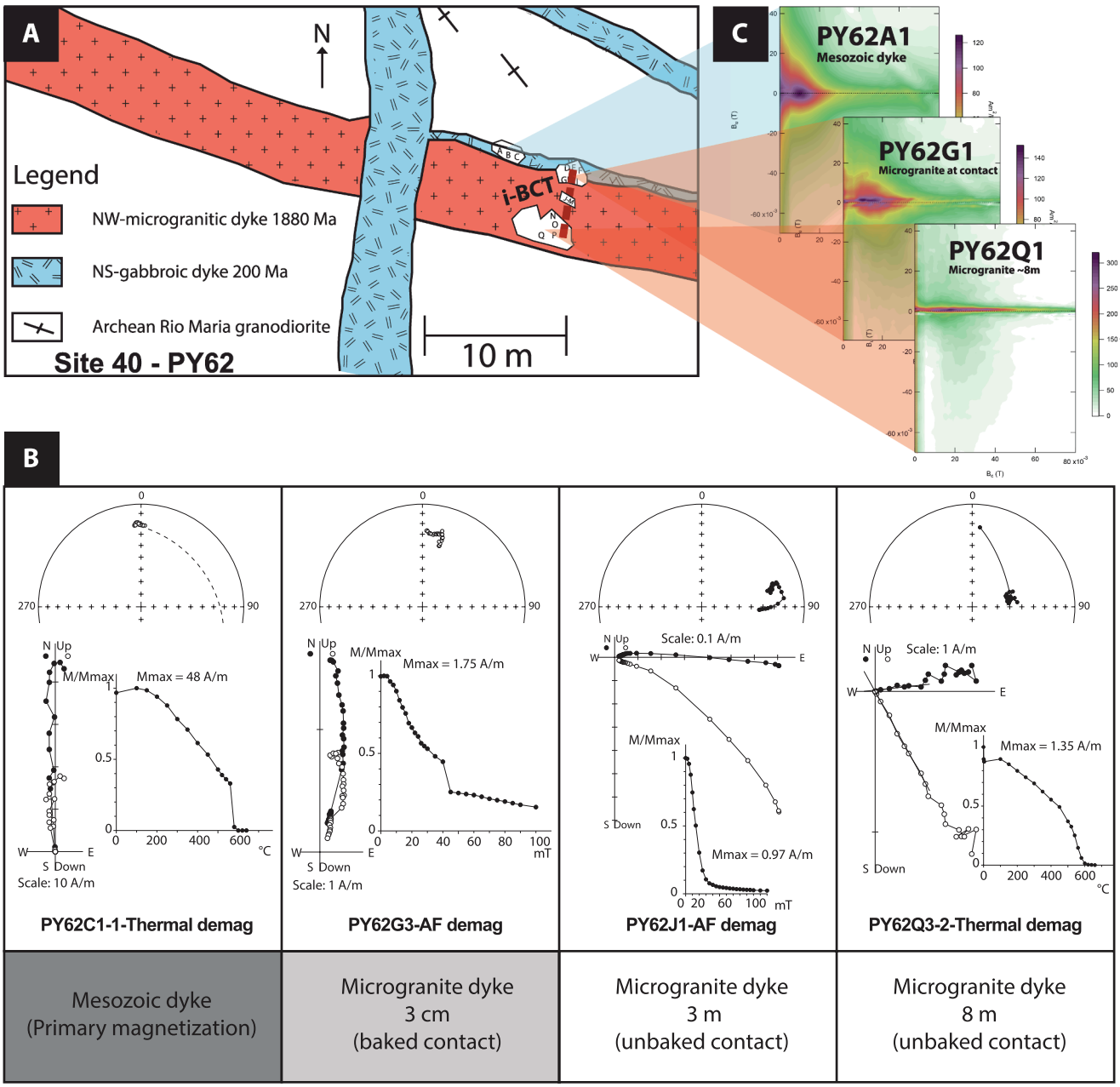

Fig. 9. Inverse baked contact test (i-BCT), showing in A: a Schematic sketch of a microgranitic dyke intersected by a NS Mesozoic gabbroic dyke, in B: FORC diagrams for samples of the Mesozoic dyke and for the microgranitic dyke at contact and far away from the contact, and in C: Stereographic projections, orthogonal projections, and normalized magnetization intensity curves for a sample of the Mesozoic dyke, and samples close to contact and far away.

7. Magnetic mineralogy

7.1. Petrography

The iron oxides were examined using a Scanning Electron Microscope (SEM) to explore their primary character. Accessory minerals in microgranitic and andesitic dykes are zircon, magnetite and titanite (*cf.* also (Dall'Agnol et al., 1997)). Magnetite (Fe_3O_4) is the primary main iron oxide and is present in all studied rocks. For example, iron oxide inclusion within an albite crystal is observed in sample PY65, suggesting a primary origin (Fig. 10-A). The EDS spectrum shows that the mineral is iron oxide (without Ti), which may be magnetite or hematite, since we cannot see the difference between Fe^{2+} and Fe^{3+} using SEM technique (Fig. 10-A). Although, magnetite grains exhibit a very small size (~5–10 μm), it was possible to detect the primary character of octahedral magnetite within a quartz phenocryst (Fig. 10-B). The EDS spectrum confirmed that this mineral is an iron oxide (Fig. 10-B). Hematite (αFe_2O_3) crystallized after a process of alteration and is responsible for the characteristic red color of the rocks (Boone, 1969; Nédélec and Bouchez, 2015; Nédélec et al., 2015). The presence of hematite is difficult to be directly observed with the microscope because the grains are very small. Ilmenite ($FeTiO_3$) in association with titanium oxide (TiO_2) and a large magnetite grain with exsolution of ilmenite were observed in an andesitic dyke (PY32 - Fig. 10-C). Magnetite grains showing exsolution of ilmenite are also present in the basaltic dykes in association with primary minerals as apatite or baddeleyite, and different types of sulfides (sphalerite, pyrrhotite) (Fig. 10-D).

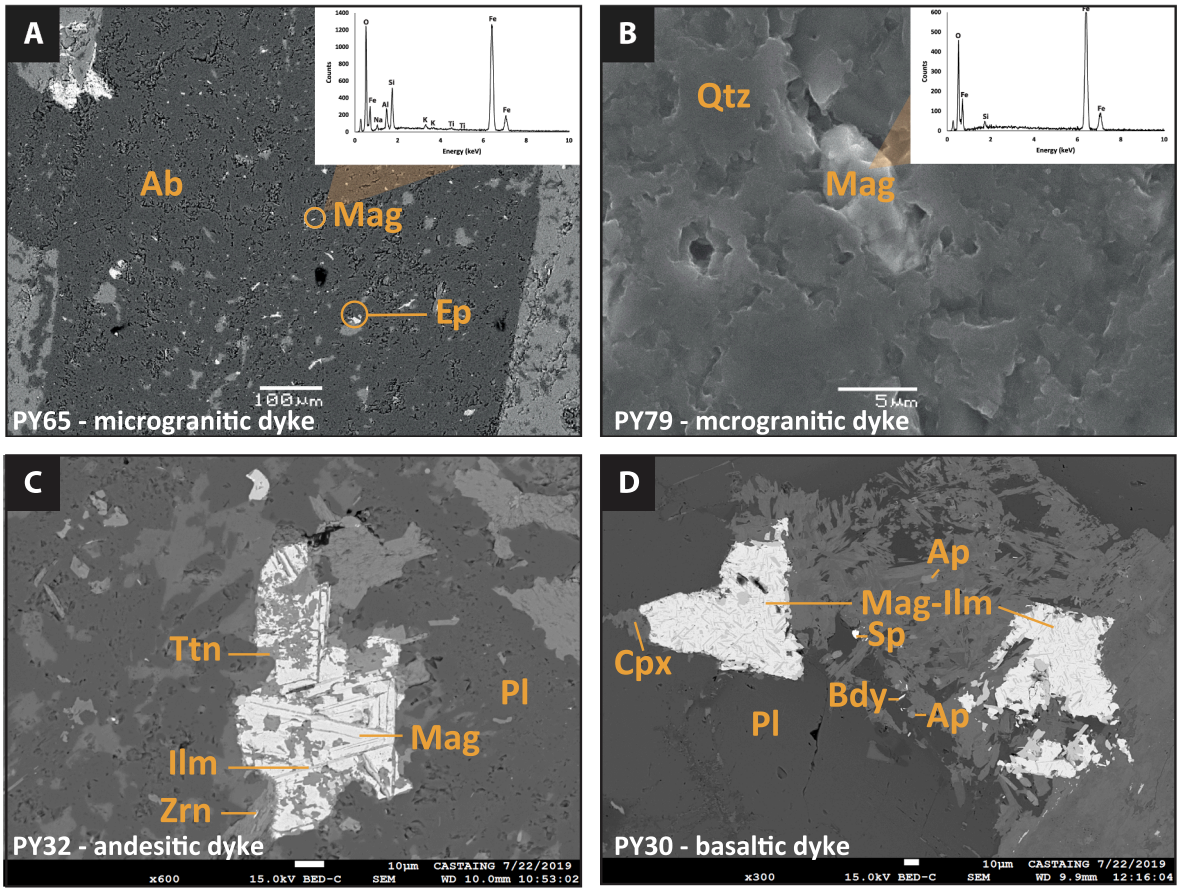

Fig. 10. Petrography of paleomagnetic samples. A: SEM-BSE micrograph of plagioclase for a microgranitic dyke (PY65) showing inclusion of primary Fe-Ti oxides and EDS spectra associated. B: SEM-BSE micrograph of primary magnetite in inclusion in a quartz crystal for a microgranitic dyke (PY79) with EDS spectra associated. C: SEM-BSE micrographs for an andesitic dyke and D for a basaltic dyke. *Mineral abbreviations*: Ab (albite), Ap (apatite), Bdy (baddeleyite), Cpx (clinopyroxene), Ep (epidote), Ilm (ilmenite), Mag (magnetite), Pl (plagioclase), Qtz (quartz), Sp (spharelite), Ttn (titanite), Zrn (zircon), from Whitney and Evans (2010).

7.2. Day's plot and hysteresis curves

Magnetic mineralogy study of most of dykes indicates that magnetization is carried by PSD magnetite (or more precisely in a vortex state (Roberts et al., 2017)) according to the Day's diagram (Fig. 11-A). For microgranite dykes, PSD magnetite is formed during the magmatic stage, so it is primary. Hematite is formed by hydrothermal alteration of the magnetite in subsolidus condition. Presence of hematite in these dykes is confirmed by hysteresis curves showing a wasp-waisted behavior and IRM curves, which do not reach saturation at fields up to 3 T (Fig. 11-B). We can observe dominance of the magnetic contribution in hematite for some microgranite dykes using the Kruiver's analysis (Kruiver et al., 2001) with ~65% of the hematite component versus 35% of the magnetite component (rich-hem) (Fig. 11-B). Magnetic mineralogy for most of microgranitic and andesitic dykes, however, is dominated by presence of magnetite rather than hematite (Fig. 11-C). Magnetic mineralogy for the NW-basaltic dykes shows that magnetization is carried by PSD magnetite (Fig. 11-D). The NS-gabbroic dyke of CAMP has also PSD magnetite as can be seen in the Day's plot (Fig. 11-A) and in the FORC diagram (Fig. 9-C). The *ca.* 2872 Ma Rio Maria granodiorite is the main basement rock in the Tucumã region (Avelar et al., 1999), and magnetic mineralogy shows large magnetite grains associated with recrystallization (Santos and Oliveira, 2016). According to the Day's plot, samples of granodiorite are mainly multidomain grains (MD) with Hcr/Hc ratios greater than 5 (see supplementary data 4 for Day plot values). So, it is very suspicious that these Archean rocks could retain a primary magnetization.

7.3. Thermal susceptibility

The thermomagnetic curve for a microgranite dyke (PY59A) shows the presence of a well-pronounced Hopkinson peak, Curie temperature around 580 °C, and the Verwey transition at low temperatures, which are characteristics of SD/PSD magnetite (Dunlop and Özdemir, 1997) as the main magnetic carrier in this rock (Fig. 12-A). Rich-hematite sample in the Day's diagram shows a curve with irreversible behavior characterized by different trajectories during heating and cooling and small fall around 600° C indicating the presence of magnetite in small quantity (Fig. 12-B). The presence of hematite, well-characterized in the previous topics, is not visible on the thermomagnetic curves, which is normal due of its low magnetic susceptibility, compared to that of magnetite. Also, during heating, a new magnetically strong mineral (probably magnetite) is being formed, possibly by alteration of other Fe-rich minerals. The NW basaltic dyke (PY71) does not show the Verwey transition but a fall at *ca.* 580 °C indicates the presence of magnetite (Fig. 12-C). The Jurassic dyke PY60L shows a reversible behavior with a well-pronounced Hopkinson peak, Curie temperature at about 580 °C, as well as the Verwey transition at low temperatures, which are characteristics of SD/PSD magnetite (Fig. 12-D).

8. Discussion

8.1. Reliability of paleomagnetic poles

8.1.1. CA1 paleomagnetic pole

The CA1 grand mean pole was calculated using 26 sites having ChRM

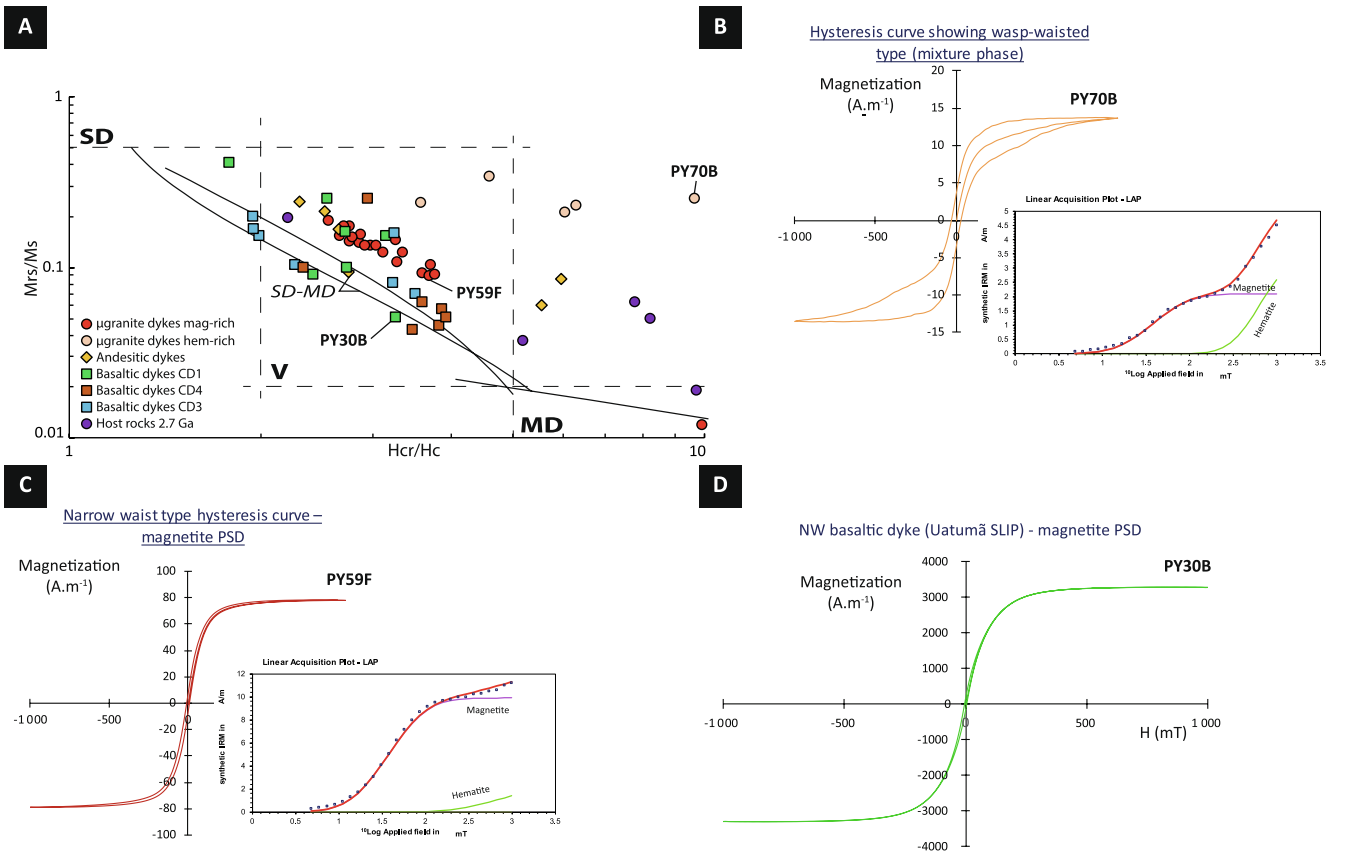

Fig. 11. A: Day plot (Day et al., 1977) of the hysteresis ratios Mrs/Ms and Hcr/Hc for samples analyzed in this study. B: Hysteresis curve for a hematite-rich microgranite with IRM decomposition (PY70B). C: Hysteresis curve for a magnetite-rich microgranitic sample (PY59F). The strong magnetite component is well-observed in the IRM decomposition. D: Hysteresis curve of a typical sample of a basaltic dyke (PY30B) where the magnetic carrier falls in the Pseudo Single Domain of the Day's diagram (magnetite).

directions with steep upward and downward inclinations. Among these 26 sites, 16 sites are basaltic, andesitic and microgranitic dykes of the Carajás Province (this study) and 10 sites are from the coeval volcanic rocks of the São Felix do Xingu area (Antonio et al., 2017). CA1 component is carried by stable hematite in the rhyolitic rocks of São Felix do Xingu area and PSD magnetite in basaltic dykes of Tucumã and Rio Maria areas. The CA1 pole (328.7°E, 23.3°S, A_{95} = 8.7°) satisfies 6 (Q = 6) out of the 6 quality criteria proposed by Van der Voo (1990), if we discard his seventh criterion as suggested in the Paleomagia database for Precambrian rocks (Pivarunas et al., 2018; Veikkolainen et al., 2017b): (1) the four U-Pb dating on apatite and one U-Pb age on zircon from andesitic and basaltic dykes (this study) yielded consistent ages around 1880 Ma, and paleomagnetic analysis on the same dykes revealed similar ChRM directions. These ages are concordant with two U-Pb baddeleyite ages (1880 ± 2 Ma, 1885 ± 2 Ma) determined on two other basaltic dykes in the Rio Maria area (Teixeira et al., 2019b), and two zircon U-Pb ages (1882 ± 4 Ma, 1881 ± 3 Ma) obtained for two microgranitic dykes (Silva et al., 2016). The weighted average age of ten well-dated paleomagnetic sites used in the CA1 grand mean pole (see Fig. 7-B) is 1881.4 ± 2.5 Ma (MSWD = 3.9), which constrain the age of the CA1 component. The multi-method radiometric dating (U-Pb baddeleyite, zircon and apatite) show that the magnetic age is clearly close to the crystallization age of these rocks. Also, the blocking temperatures (300–500 °C) associated with the apatite isotopic system demonstrate that no later high thermal (>300 °C) perturbation occurred in the CA1 dykes. (2) The CA1 pole was calculated with 26 sites and 248 specimens and show good Fisher's statistical parameters (A_{95} = 8.7°, K = 11.7) (Table 4). (3) Remanence vectors were well-isolated using stepwise AF treatments, and thermal demagnetizations. They were calculated by the principal component analysis (Kirschvink, 1980) through the visualization of magnetic directions plotted in the Zijderveld diagrams and stereographic projections. (4) A positive inverse baked contact test obtained for a Jurassic dyke cutting a 1880 Ma microgranitic dyke in the Tucumã area (Fig. 9), shows that the CA1 remanent magnetization is older than ~199 Ma. Another positive inverse baked contact obtained in São Felix do Xingu for a ~1855 Ma microgranitic dyke cutting the andesitic rock from the 1880 Ma Sobreiro Formation demonstrates that CA1 component is older than 1855 Ma, and most probably it was acquired at the time rock was formed at 1880 Ma (Antonio et al., 2017). (5) The fact that the same paleomagnetic results were disclosed for volcanic rocks of the São Felix do Xingu area and the Carajás dyke swarm in Tucumã and Rio Maria areas, some 300 km apart implies that no tilting affected these rocks after their emplacement, at least between the studied areas. Moreover, these two areas must belong to the same geological province and a separation into different geological domains as proposed by Vasquez et al. (2008) is no longer sustainable. (6) The CA1 component pass a reversal test, which implies the secular variation was averaged out. (7) Even if we discard this criterion, the CA1 pole is different from poles calculated for younger units in the Amazonia craton according to the compiled Precambrian Paleomagnetic database for Amazonia by D'Agrella-Filho et al. (2016) (see also Antonio et al. (2017). The southeastern part of the Amazonia craton, was cut by the ~535 Ma mafic dykes coeval to the Araguaia Belt and the ~200 Ma Central Atlantic Magmatic Province (CAMP) (Teixeira et al., 2019b). No paleomagnetic study is presently available for the ~535 Ma dykes but the CA1 direction is different from the Puga B pole (Q = 2), whose age is estimated to be ~520 Ma (Trindade et al., 2003) and from the CAMP paleomagnetic poles (Moreira 2019). So, the 1880 Ma CA1 paleomagnetic pole can be considered as a key pole.

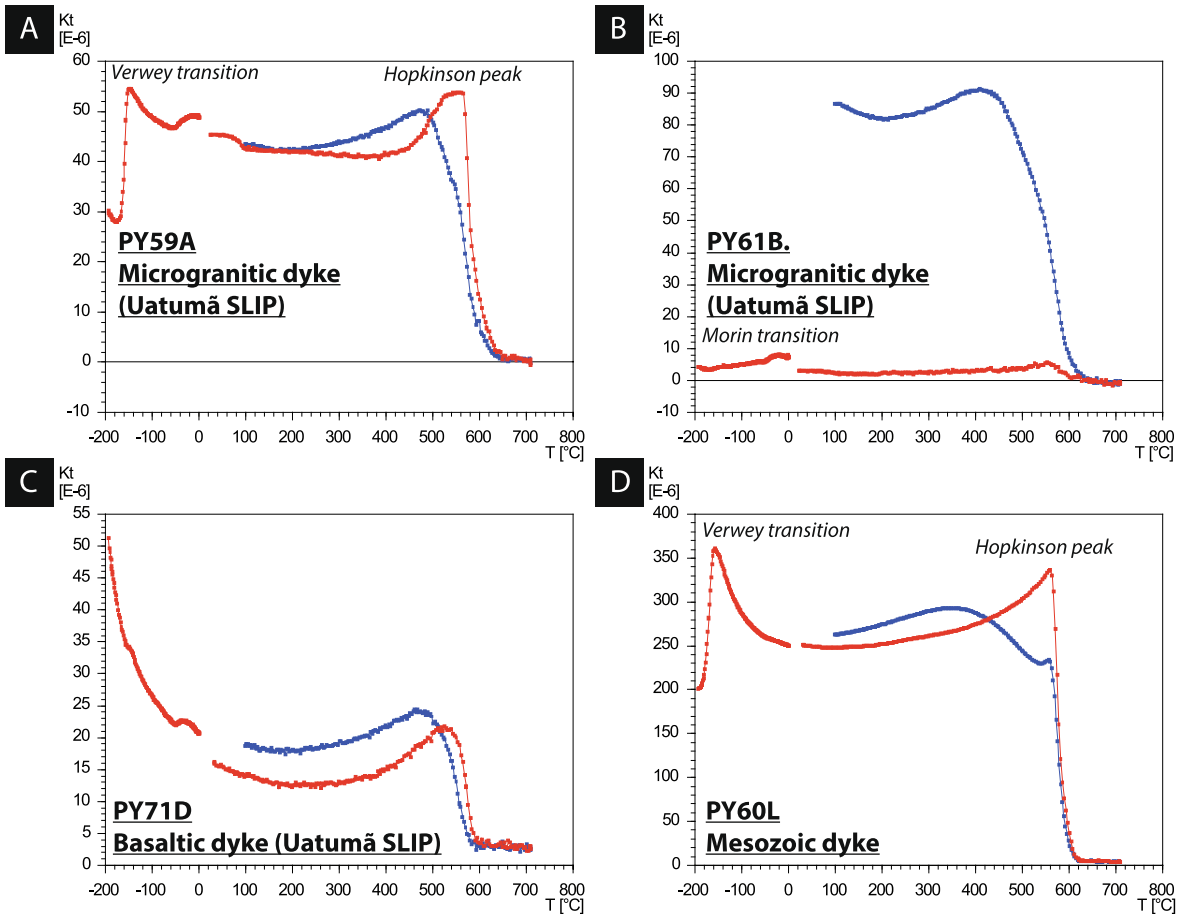

Fig. 12. A: Example of thermomagnetic curves for a micrograniticdyke with a strong component of magnetite (PY59A). B: Example of thermomagnetic curve for a micrograniticdyke where hematite is dominant in magnetic mineralogy (PY61B). C: Thermomagnetic curve for a NW basaltic dyke dated at ~1880 Ma in this study. D: Typical thermomagnetic curve for the Mesozoic dykes.

8.1.2. CA2 paleomagnetic pole

Only 3 out of the 18 sites used to calculate the CA2 grand mean pole are from this work. This component is better represented at the São Felix do Xingu (15 sites) than at Tucumã or Rio Maria areas. The three sites of Archean host rocks that have the same magnetization are not considered in the CA2 grand mean pole calculation. These sites suggest that an important geological regional event affected these rocks imprinting this component in these Archean rocks. We suggest that it is represented by the last pulse of the Uatumã magmatic event (the Velho Guilherme Suite intrusions) occurred at ~1855 Ma as indicated by a positive baked contact test made for a micrograniticdyke from the Velho Guilherme Suite (dated at 1855 Ma) cutting the andesitic rock from the 1880 Ma Sobreiro Formation in the São Felix do Xingu area (Antonio et al., 2017). As for the CA1 component described above, the grand mean pole CA2 satisfies also 6 of the first 6 quality criteria of Van der Voo (1990): (1) The Velho Guilherme dykes are well-dated at 1853.7 ± 6.2 Ma by LA-ICP-MS U-Pb zircon (Antonio et al., 2017), and 1857 ± 8 Ma by SHRIMP U-Pb zircon (Roverato, 2016) which well-constrain the age of CA2 component. One age of 1903 ± 13 Ma by U-Pb zircon and one age of 1885 ± 30 by U-Pb apatite were obtained in this study for one micrograniticdyke. The U-Pb apatite age could be considered more reliable for the magnetic age, within error similar to the ~1860 Ma age of the Velho Guilherme suite (2) The CA2 paleomagnetic pole was calculated using 18 sites and 132 specimens and have good statistical parameters (A_{95} = 8.8°, K = 16.2). (3) As for component CA1, stepwise AF and thermal demagnetizations were used to separate the CA2 component, which was calculated by the principal component analysis (Kirschvink, 1980). (4) No baked contact test in the Rio Maria and Tucumã areas was performed but a positive baked contact test was described in the São Felix do Xingu area for a 1855 Ma micrograniticdyke of the Velho Guilherme suite at the contact with the Sobreiro Formation (Antonio et al., 2017). (5) No deformation or metamorphism was observed in micrograniticdykes. Unless some dyke intrusions at *ca.* 535 Ma, related to the marginal Brasiliano Araguaia belt development, and at *ca.* 200 Ma, related to the CAMP event, the Carajás Domain maintained its tectonic integrity since 1850 Ma. Although the 2870 Ma host rocks revealed also the same component, this is interpreted to be due to a regional remagnetization during the last pulse of the Uatumã event at ~1855 Ma. With an extension >1.500.000 km^2, the Uatumã SLIP and its thermal footprint have the potential to induce a regional remagnetization. (6) Two polarities were observed, which implies that secular variation was average out. (7) Although the seventh criterion of Van der Voo (1990) may be disregarded for Precambrian rocks (see above), it is obeyed by this component, since it doesn't have any similarity with younger paleomagnetic data available for the Amazonia craton. So, the CA2 grand mean pole can be considered as key (Q = 6) with an age of ~1855 Ma.

8.2. CD3 and CD4 paleomagnetic poles

Other two components (CD3 and CD4) were isolated in the investigated rocks. The CD3 single normal polarity component was disclosed for 8 well-known Jurassic dykes dated at 199.3 ± 0.3 Ma (Moreira, 2019; Nomade et al., 2000). A positive baked contact test for one of these dykes supports a primary magnetization for it (Fig. 9). The CD3 pole (Q = 5) calculated for the CAMP dykes in Carajás is located at

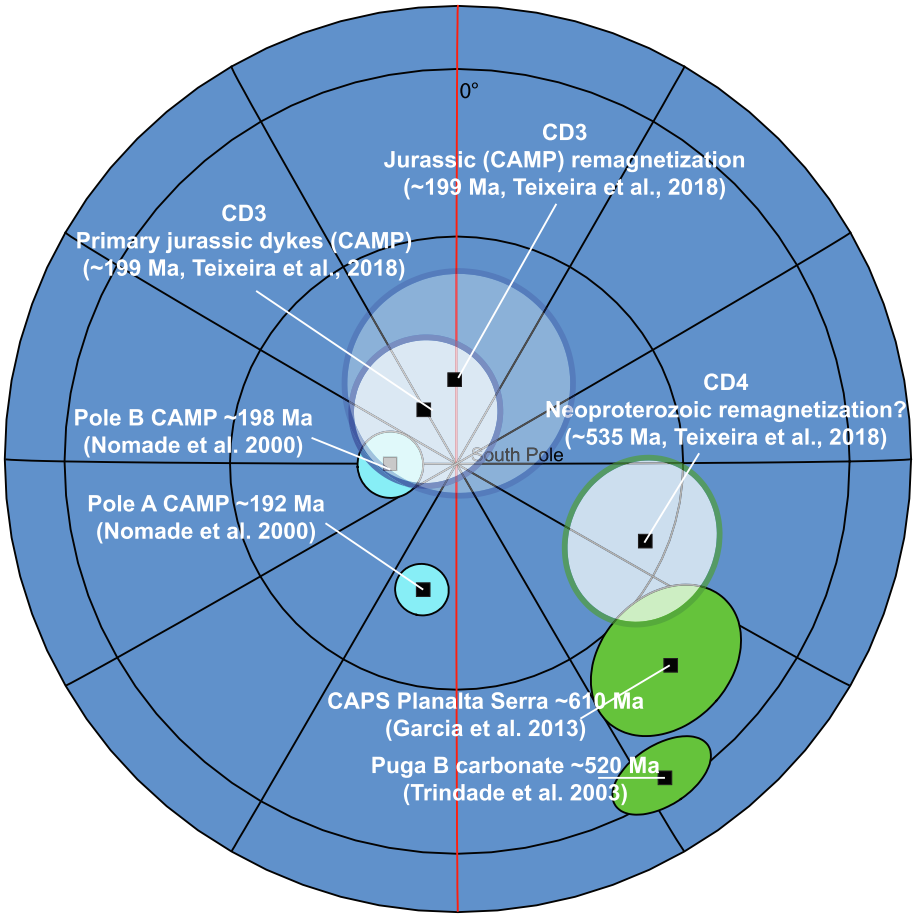

Fig. 13. A: Comparison of the primary CD3 and re-magnetized paleopoles (this study) with reference paleomagnetic poles obtained for rocks from the ~200 Ma Central Atlantic Magmatic Province (CAMP) – Amazonia (Nomade et al., 2000). Comparison of the CD4 paleopole with previous Neoproterozoic data (~610–520 Ma) (Garcia et al., 2013; Trindade et al., 2003).

82.3°S, 325.6°E (A_{95} = 9.5°, K = 35). Although more scattered, the CD3 secondary directions disclosed for the older rocks (Fig. 8-B) yielded a paleomagnetic pole (79.8°S, 359.4°E; A_{95} = 14.6°, K = 13.3) very similar to the CAMP CD3 pole. These poles statistically agree with another pole determined for the CAMP dolerite dykes, in French Guana, and dated at 198 Ma (Fig. 13; (Nomade et al., 2000)). It is also similar to a recent paleomagnetic pole obtained for the ~201 Ma Penatecaua sills (76.5°S, 279.5°E, A_{95} = 3.8°) sampled *ca.* 700 km far from Carajás (Moreira 2019).

The CD4 paleomagnetic pole was calculated for 11 basaltic and microgranitic dykes in Carajás and is located at 63.4°S, 113.7°E (A_{95} = 10.8°, K = 18.7). No age is presently available for these dykes, or field tests to constrain the age of the CD4 pole. We suggest it represents a younger regional remagnetization for the following reasons: (1) this component is observed on five 1880 Ma microgranitic dykes – the primary component of the 1880 Ma magmatic event is probably represented by pole CA1 as discussed above; (2) this component looks like the SF3 component (40.7°S, 128.8°E, A_{95} = 15.6°) observed in the ~1880 Ma volcanic rocks in SFX (Antonio, 2017). This component is carried by large magnetite in coarse-grained microgranite, and goethite in rhyolite as secondary component (Tb < 200 °C) (Antonio et al. (2017). (3) The CD4 pole is close to the Neoproterozoic/Cambrian Amazonian paleomagnetic poles (see Fig. 13): the Planalto da Serra Alkaline Complex (49.7°S, 133.4°E, A95 = 10.8°) (Garcia et al., 2013) whose age is established by several Ar-Ar ages on phlogopite at *ca.* 610 Ma (D'Agrella Filho et al., 2018; De Min et al., 2013) and the secondary Puga B pole (33.6°S, 146.9°E, A95 = 8.4°) (Trindade et al., 2003) for which the authors attributed an age of ~520 Ma.

8.3. *Geological model and Paleoproterozoic APW path for Amazonia and West Africa*

Geological data suggest a connection between Amazonia (Am) and West Africa (WA) cratons after the "Transamazonian/Eburnean" collisional events at *ca.* 2100–2000 Ma (Caen-Vachette, 1988; Ledru et al., 1994; Vanderhaeghe et al., 1998). First paleomagnetic data for West Africa and Amazonia highlighted the reassessment of the Pangea fit which would not be valid before the Neoproterozoic (Onstott and Hargraves, 1981). These reconstructions suggested a rotation of about 30° of the Amazonia in relation to West Africa to align the Guri (Am) and Sassandra (WA) shear zones (Caen-Vachette, 1988; Cohen and Gibbs, 1989; Feybesse and Milési, 1994; Ledru et al., 1994). More recently, new paleomagnetic data seem to support these reconstructions (Fig. 14-A, option A) (Bispo-Santos et al., 2014a; Nomade et al., 2003). However, a recent revision of structures and kinematics of the Transamazonian-Eburnean orogen by Chardon et al. (2020) allow to re-align the Eburnean strain pattern in West Africa with large Transamazonian shear corridors in the Guiana Shield, which avoids inconsistencies in structural patterns in previous models (Bispo-Santos et al., 2014a; Grenholm, 2019; Nomade et al., 2003). In this new model (Fig. 14-B, option B), the Sassandra shear zone is no longer connected to the Guri shear zone, but with the North Guiana Through (Ledru et al., 1991). These West African and Amazonian shear zones, named as the Burghana-Transamazonian mega shear zone by Chardon et al. (2020), are connected to the Pisco-Juruá shear zone which is the most rectilinear corridor in Guiana Shield (Chardon et al., 2020).

Here, we re-evaluate the paleomagnetic data and APW paths for

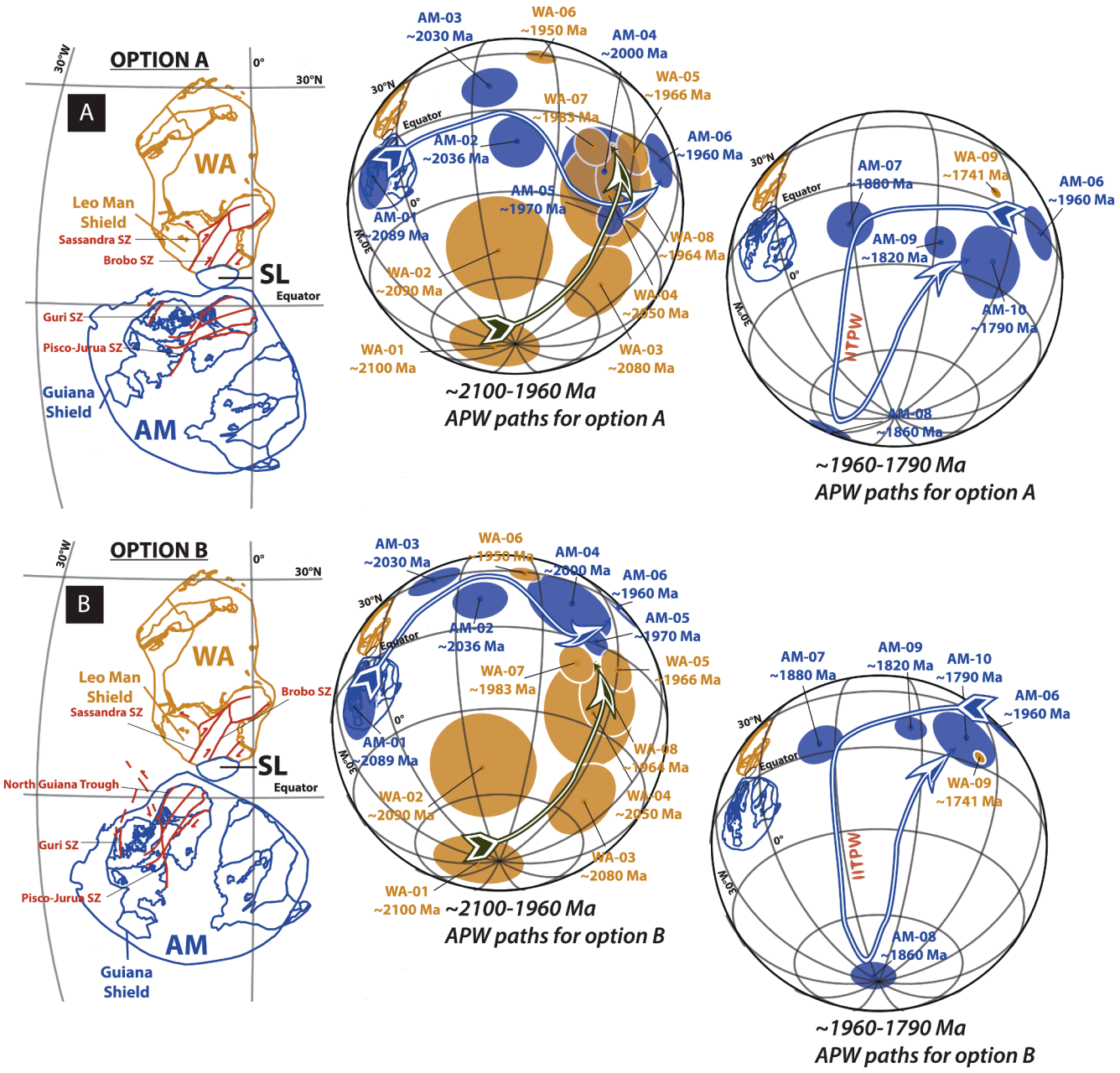

Fig. 14. A: Option A for the Amazonia-West Africa connection, using a geological connection between the Guri (Amazonia, AM) and Sassandra (West Africa, WA) shear zones (Bispo-Santos et al., 2014a; Nomade et al., 2003). The apparent polar wander paths (APWPs) for Amazonia and West Africa between ~2100 and 1960 Ma and between ~1960 and 1790 Ma are illustrated for option A in the two orthographic projections. SL is the São Luis craton associated to West Africa. Euler pole for option A (fixed West Africa): lat: 61.09°; long: −19.63°; angle: 57.5°. B: Option B for the Amazonia-West Africa connection, connecting the North Guiana Trough with the Sassandra shear zone as suggested by Chardon et al. (2020). The apparent polar wander paths (APWPs) for Amazonia and West Africa between ~2100 and 1960 Ma and between ~1960 and 1790 Ma are illustrated for option B in the two orthographic projections. Euler pole for option B (fixed West Africa): lat: 33.98°; long: −28.42°; angle: 73.96°. TPW at ~1880–1850 Ma is indicated in red by discordance between CA1 and CA2. Paleomagnetic poles used are listed in Table 5. (For interpretation of the references to color in this figure legend, the reader is referred to the web version of this article.)

Amazonia and West Africa according to these models (Table 5; Fig. 14). According to Klein and Moura (2008), the São Luis craton in Brazil was part of the West African craton during the Paleoproterozoic and it was not considered by Bispo-Santos et al. (2014a) in their reconstruction. Based on the new structural pattern for the Transamazonian-Eburnean orogen proposed by Chardon et al. (2020), the new alternative model (Option B) is compatible with the available paleomagnetic data between ~2100–1960 Ma (Fig. 14-B). Obviously, the option A cannot be rejected on paleomagnetic grounds due to the quality of the APW paths. Note that using the new configuration (Fig. 14-B), the ~1790 Ma Avanavero pole for Amazonia (Bispo-Santos et al., 2014b) overlaps the ~1740 Ma PGV obtained for the Iguarda dykes of West Africa (Neres et al., 2016) which can give a suggestive support for option B. It should be noted that this result could also be a coincidence because the age match is ~50 Ma different. Excursion of the APW path at *ca.* 1860 Ma and return to broadly the same place at *ca.* 1820 Ma is consistent with a TPW oscillation (Creveling et al., 2012). This new configuration seems to support the viability of a long-lived paleomagnetic connection between these two units.

The option A configuration is close to the hypothesized position of Amazonia and West Africa in the (South-America-Baltica) SAMBA connection (Johansson, 2009). If option B indeed proves more viable,

Table 5
Paleomagnetic poles compilation for West Africa and Amazonia and West Africa used in Fig. 14. Nominal age is the magnetic age associated to the paleomagnetic pole. Confidence column indicate the geochronological method (strat: stratigraphic correlation, Pb-Pb method, APWP: correlation using APW path, Rb-Sr isochron, U-z: U-Pb zircon, U-b: U-Pb baddeleyite, U-a: U-Pb apatite, A-h: Ar-Ar amphibole, A-bi: Ar-Ar biotite) and possible field test (i-BCT: inverse baked contact test, BCT: baked contact test). *References*: (1) (Nomade et al., 2003), (2) (Piper and Lomax, 1973), (3) (Sabaté and Lomax, 1975), (4) (Peucat et al., 2005), (5) (Onstott et al., 1984b), (6) (Onstott and Dorbor, 1987), (7) (Neres et al., 2016), (8) (D'Agrella-Filho et al., 2011), (9) (Nomade et al., 2001), (10) (Théveniaut et al., 2006), (11) (Bispo-Santos et al., 2014a), (12) (Onstott et al., 1984a), (13) (Bispo-Santos et al., 2014b).

Code	Name	A_{95}	Plat (°N)	Plong (°E)	Nominal Age (Ma)	Confidence	References
West Africa							
WA-01	IC1 Ivory Coast intrusions	16.1	−82	292	2100	strat.	1
WA-02	PL1 Obuasi greenstone	19	−50	36	2090	U-z	2
WA-03	PL2 Abouasi-Obuasi Dolerite intrusions	14	−53	102	2080	strat.	2
WA-04	IC2 Ferke batholith -Ivory coast	18.9	−25	83	2050	Pb-Pb APWP	1
WA-05	GAF Aftout granite	7.8	−6	90	1966	strat. U-z	2, 3, 4
WA-06	SL Aftout gabbro	5.7	28.8	55.1	1950	strat. Rb-Sr, U-z	3, 4
WA-07	AH Harper amphibolite	7	−10	73	1983	A-h	5
WA-08	OD Liberia Granulite	13	−17.5	89	1964	Rb-Sr	6
WA-09	Iguerda Inlier dikes	2.5	−4	262.1	1741	U-z	7
Amazonia							
AM-01	Mean GF1 (Approuague granite)	11.2	1.8	292.5	2089	U-z, i-BCT	8, 10
AM-02	OYA Oyapok tonalite and meta-ultrabasite	9.9	−28	346	2036	U-z	9
AM-03	ARMO, Armontabo River tonalite	10.1	−2.7	346.3	2030	i-BCT	10
AM-04	Mean CA1 (Imataca-Encrucijada)	16.5	−42.9	21.9	2000		11
AM-05	Mean GF2 Coastal late monzogranite	5.8	−58.5	30.2	1970		8
AM-06	Surumu volcanics	10.1	−27.4	54.8	1960	U-z, i-BCT	11
AM-07	**POLE CA1**	8.7	−23.3	328.7	1880	U-a, U-z, i-BCT	**This study**
AM-08	**POLE CA2**	8.8	−30.2	221.3	1860	U-a, U-z, BCT	**This study**
AM-09	ARO Guaniamo dikes (Comp II)	6	−42	0	1820	A-bi	12
AM-10	Avanavero sills	13	−48.4	27.9	1789	U-b, i-BCT	13

then the SAMBA connection of these two cratons relative to Baltica needs to be revised in the paleogeographic models.

8.4. Geophysical anomalies: weak dipolar field or true polar wander event?

According to our results, two paleomagnetic poles are considered as primary for the Amazonia craton: the CA1 pole dated at 1880 Ma and the CA2 pole dated at 1860 Ma. These almost coeval, but very discordant paleomagnetic poles (Fig. 14), supposedly of primary origins, would imply in a great drift for proto-Amazonian craton which is unrealistic for the current plate tectonics. So, some alternative interpretations are discussed here that could explain such inconsistence:

(1) *Possibility of local vertical-rotation axis due to shear zones and deformation along orogens can provide discordant coeval paleomagnetic poles.* For the Slave craton, Mitchell et al. (2010) suggested that the oscillations in almost coeval paleomagnetic poles (1960–1870 Ma) that define the Coronation APWP loop can be explained by true polar wander (TPW) events. Recently, however, Gong et al., (2018) revised the inconsistent paleomagnetic data obtained for the Pearson Formation (~1870 Ma) for small blocks in the Great Slave Basin, and suggested that it can be explained by a rotation of *ca.* 60° along local vertical-rotation axis in the area, originating by fault displacements (Gong et al., 2018). These authors suggest that some other broadly coeval paleomagnetic poles in the Great Slave Supergroup could have been also affected by local rotations, *e.g.*, the aberrant poles of the Stark and Tochatwi Formations (Bingham and Evans, 1976; Evans and Bingham, 1976), although no geological evidence is yet available to confirm this hypothesis. Concerning the Carajás area in this study, CA1 (1880 Ma) and CA2 (1860 Ma) ChRM directions were obtained both, for volcanic rocks from the São Felix do Xingu area and from dykes in the Rio Maria and Tucumã areas, distant up to 300 km apart. Therefore, most probably, no deformation or shear zones affected these rocks after the 1880 Ma and 1860 Ma rock intrusions. Also, as already stressed, the volcanic rocks of São Felix do Xingu is part of the Carajás Province and not a different domain as suggested by Santos (2003).

(2) *Regional remagnetization can disturb the paleomagnetic record to give discordant poles.* For Baltica, similar 1900–1750 Ma paleomagnetic poles fall into the Permian segment of the Phanerozoic APWP traced for this cratonic block, which could explain why they are tightly clustered (Bazhenov et al., 2016). It should be stressed, however, that there is a highest probability for Paleoproterozoic poles to coincide with a younger APW path for a same continent and the argument of coincidence with younger poles to justify a remagnetization is not conclusive (Pivarunas et al., 2018). In the case of the Carajás area, as stressed above, the CA1 and CA2 poles do not coincide with other younger poles from the Amazonia craton, and the positive baked contact test performed for the CA1 component prove that both CA1 and CA2 components are of primary origins.

(3) *Another explanation for discordant paleomagnetic poles could be the presence of a Weak dipolar field during Proterozoic* (Biggin et al., 2009, 2015). Recently, values ranging between 1.22 and 2.15 10^{22} Am^2 was proposed for the intensity of the geomagnetic field at ~1860 Ma based on paleointensity studies on rocks from Baltica (Veselovskiy et al., 2019). These low values seem continue until ~1790 Ma with low paleointensity data obtained for the ~1790 Ma Avanavero sills in Amazonia (Di Chiara et al., 2017) or for the ~1790 Ma Hoting gabbro in Baltica (Donadini et al., 2011). These data seem to support a weak dipolar field at least for sometimes in the interval ~1900–1700 Ma, which could be at the origin of these paleomagnetic discrepancies. So, test the validity of the Geocentric Axial Dipole (GAD) is important before using paleomagnetic data for paleogeographic reconstructions (Veikkolainen et al., 2017a). Analysis of a global compilation of paleointensity data showed the Precambrian field seems to be dominated by an axial dipole component associated to an octupolar component (Veikkolainen et al., 2017a). Global compilations for Precambrian reversal tests, including our paleomagnetic reversal test at ~1880 Ma, also agree with a dominant dipolar component for the geomagnetic field during Proterozoic (Veikkolainen et al., 2014). Thus, these results exclude the low Paleoproterozoic geomagnetic field as the reason for the CA1 and CA2 poles discrepancy.

(4) *If discordant paleomagnetic poles are primary, another explanation is to suppose the motion of the entire solid earth (mantle + crust) in respect to the spin axis of the Earth, the true polar wander (TPW) hypothesis* (Raub et al., 2007). The two TPW events, before and after *ca.* 1860 Ma comprising the full oscillation is close to ~90° in amplitude (Fig. 14), *i.*

e., inertial interchange true polar wander (IITPW) (Goldreich and Toomre, 1969; Kirschvink et al., 1997; Rose and Buffett, 2017). The 1900–1800 Ma time interval is associated with worldwide Large Igneous Provinces (LIPs) emplaced in all cratons, and paleomagnetic studies were carried out for many of these LIPs. A compilation of the almost coeval, but discordant paleomagnetic poles was performed by Antonio et al. (2017). Some geological and paleomagnetic associations of this model is well-established like the connection between India and Australia (Liu et al., 2018; Stark et al., 2019). Despite the small amount and quality of paleomagnetic data, Antonio et al. (2017) conclude that the hypothesis of a True Polar Wander event at ~1880–1850 Ma is the best explanation for these discordant paleomagnetic poles.

9. Conclusion

The first U-Pb apatite ages for andesitic, basaltic, and microgranitic dykes were obtained for the Carajás Province (Amazonia craton). These new U-Pb apatite ages of ~1890–1850 Ma agree from previous zircon and baddeleyite ages for the Carajás dyke swarm which belong to the Uatumã event (Antonio et al., 2017; Teixeira et al., 2019b). Two key paleopoles, CA1 (~1880 Ma; 23.3°S, 328.7°E, A_{95} = 8.7°) and CA2 (~1855 Ma; 30.2°S, 221.3°E, A_{95} = 8.8°), were calculated for the Carajás volcanic rocks and dyke swarms. They are proven to be primary by a positive baked contact test for a ~1855 Ma granodioritic dyke (component CA2) in contact with the andesitic rock (CA1 component) from the 1880 Ma Sobreiro Formation, reinforced by the U-Pb multi-method radiometric dating (zircon, baddeleyite, apatite) which indicates that no high thermal events (>300 °C) affected the rocks after their intrusion. Two younger paleomagnetic poles (CD3 and CD4) were also obtained: a *ca.* 200 Ma pole (CD3 pole) for Jurassic dykes from Carajás is located at 82.3°S, 325.6°E (A_{95} = 9.5°); the CD4 pole (63.4°S, 113.7°E, A_{95} = 10.8°) was obtained for some of the dykes and basement rocks whose age is yet undefined. A revision of the Paleoproterozoic APW paths for Amazonia and West Africa supports a new geological configuration between these two cratons (Chardon et al., 2020) which allows to restore the Sassandra shear zone in West Africa with the North Guiana Through and other shear zones in Guiana Shield. The discrepancy in the ~1890–1850 Ma paleomagnetic poles observed in several cratons in the world could be better explained by a true polar wander event. However, new good-quality paleomagnetic data is necessary to resolve this issue.

CRediT authorship contribution statement

P.Y.J. Antonio: Conceptualization, Methodology, Investigation, Writing - original draft, Visualization. **M.S. D'Agrella-Filho:** Supervision, Funding acquisition. **A. Nédélec:** Supervision, Funding acquisition. **M. Poujol:** Investigation, Methodology. **C. Sanchez:** Investigation, Methodology. **E.L. Dantas:** Investigation, Methodology. **R. Dall'Agnol:** Validation. **M.F.B. Teixeira:** Investigation, Validation. **A. Proietti:** Investigation, Validation. **C.I. Martínez Dopico:** Investigation. **D.C. Oliveira:** Investigation. **F.F. Silva:** Investigation. **B. Marangoanha:** Investigation. **R.I.F. Trindade:** Funding acquisition, Supervision.

Declaration of Competing Interest

The authors declare that they have no known competing financial interests or personal relationships that could have appeared to influence the work reported in this paper.

Acknowledgements

We thank the Prof. W. Teixeira, the careful contribution of R. Mitchell, and one anonymous reviewer for constructive comments on the manuscript. We thank the Universidade Federal do Pará (UFPA) for the field trip logistical support and FAPESP (grants 2012/20335-4, 2013/22957-5, 2016/13689-5, 2017/18840-6) for financial support. RD acknowledge support from Conselho Nacional de Desenvolvimento Científico e Tecnológico (CNPq; Proc. 306108/2014-3 and 304648/2019-1) and the Instituto Nacional de Ciência e Tecnologia de Geociências da Amazônia/Geociam (CNPq-FAPESPA-CAPES-PETROBRAS, Proc. 573733/2008-2).

Appendix A. Supplementary data

Supplementary data to this article can be found online at https://doi.org/10.1016/j.precamres.2020.106039.

References

Almeida, F.F.M., Hasui, Y., Neves, B.B.D., Fuck, R.A., 1981. Brazilian structural provinces: an introduction. Earth Sci. Rev. 17, 1–29.
Amaral, G., 1974. Geologia Pré-Cambriana da região amazônica. Universidade de São Paulo.
Antonio, P.Y.J., 2017. Paleomagnetism and petrogenesis of Paleoproterozoic units from the Uatumã event in the northern Amazonian Craton, Tese de Doutorado, Instituto de Astronomia, Geofísica e Ciências Atmosféricas (IAG) and Geosciences et Environnement Toulouse (GET). Universidade de São Paulo and Universite Toulouse 3 Paul Sabatier (UT3 Paul Sabatier), São Paulo and Toulouse, p. 320.
Antonio, P.Y.J., D'Agrella-Filho, M.S., Trindade, R.I.F., Nédélec, A., de Oliveira, D.C., da Silva, F.F., Roverato, M., Lana, C., 2017. Turmoil before the boring billion: Paleomagnetism of the 1880–1860Ma Uatumã event in the Amazonian craton. Gondwana Res. 49, 106–129.
Avelar, V.G., Lafon, J.-M., Correia, J.R., Macambira, F.C., 1999. O Magmatismo arqueano da região de Tucumã-Província Mineral de Carajás: novos resultados geocronológicos. Braz. J. Geol. 29, 453–460.
Bazhenov, M.L., Levashova, N.M., Meert, J.G., 2016. How well do Precambrian paleomagnetic data agree with the Phanerozoic apparent polar wander path? a Baltica case study. Precambr. Res. 285, 80–90.
Bettencourt, J.S., Juliani, C., Xavier, R.P., Monteiro, L.V.S., Bastos Neto, A.C., Klein, E.L., Assis, R.R., Leite, W.B., Moreto, C.P.N., Fernandes, C.M.D., Pereira, V.P., 2016. Metallogenetic systems associated with granitoid magmatism in the Amazonian Craton: an overview of the present level of understanding and exploration significance. J. S. Am. Earth Sci. 68, 22–49.
Biggin, A.J., Strik, G.H., Langereis, C.G., 2009. The intensity of the geomagnetic field in the late-Archaean: new measurements and an analysis of the updated IAGA palaeointensity database. Earth Planet Sp 61, 9–22.
Biggin, A.J., Piispa, E.J., Pesonen, L.J., Holme, R., Paterson, G.A., Veikkolainen, T., Tauxe, L., 2015. Palaeomagnetic field intensity variations suggest Mesoproterozoic inner-core nucleation. Nature 526, 245–248.
Bingham, D.K., Evans, M.E., 1976. Paleomagnetism of the Great Slave Supergroup, Northwest Territories, Canada: the Stark Formation. Can. J. Earth Sci. 13, 563–578.
Bispo-Santos, F., D'Agrella-Filho, M.S., Janikian, L., Reis, N.J., Trindade, R.I.F., Reis, M. A.A.A., 2014a. Towards Columbia: Paleomagnetism of 1980–1960 Ma Surumu volcanic rocks, Northern Amazonian Craton. Precambr. Res. 244, 123–138.
Bispo-Santos, F., D'Agrella-Filho, M.S., Trindade, R.I.F., Janikian, L., Reis, N.J., 2014b. Was there SAMBA in Columbia? Paleomagnetic evidence from 1790 Ma Avanavero mafic sills (northern Amazonian Craton). Precambr. Res. 244, 139–155.
Bleeker, W., 2003. The late Archean record: a puzzle in ca. 35 pieces. Lithos 71, 99–134.
Bogdanova, S.V., Gintov, O.B., Kurlovich, D.M., Lubnina, N.V., Nilsson, M.K.M., Orlyuk, M.I., Pashkevich, I.K., Shumlyanskyy, L.V., Starostenko, V.I., 2013. Late Palaeoproterozoic mafic dyking in the Ukrainian Shield of Volgo-Sarmatia caused by rotation during the assembly of supercontinent Columbia (Nuna). Lithos 174, 196–216.
Bogdanova, S.V., Gorbatschev, R., Garetsky, R.G., 2016. EUROPE|East European Craton☆, reference module in earth systems and environmental sciences. Elsevier 34–49.
Boone, G.M., 1969. Origin of clouded red feldspars; petrologic contrasts in a granitic porphyry intrusion. Am. J. Sci. 267, 633–668.
Borradaile, G.J., 1994. Low-temperature demagnetization and ice-pressure demagnetization in magnetite and haematite. Geophys. J. Int. 116, 571–584.
Borradaile, G.J., Lucas, K., Middleton, R.S., 2004. Low-temperature demagnetization isolates stable magnetic vector components in magnetite-bearing diabase. Geophys. J. Int. 157, 526–536.
Boyden, J.A., Müller, R.D., Gurnis, M., Torsvik, T.H., Clark, J.A., Turner, M., Ivey-Law, H., Watson, R.J., Cannon, J.S., 2011. Next-generation plate-tectonic reconstructions using GPlates. Geoinformatics: cyberinfrastructure for the solid earth sciences, 95–114.
M. Brown T. Johnson N.J. Gardiner Plate Tectonics and the Archean Earth Annual Review of Earth and Planetary Sciences 48 2020 p. 12.11-12.30.
Buchan, K.L., 2013. Key paleomagnetic poles and their use in Proterozoic continent and supercontinent reconstructions: a review. Precambr. Res. 238, 93–110.
Caen-Vachette, M., 1988. The West African connection: evolution of the central atlantic ocean and its Continental Margins Le craton ouest-africain et le bouclier guyanais: un seul craton au Protérozoïque inférieur? J. African Earth Sci. (and the Middle East) 7, 479–488.

Cassini, L.V., Moyen, J.-F., Juliani, C., 2020. Orosirian magmatism in the Tapajós Mineral Province (Amazonian Craton): The missing link to understand the onset of Paleoproterozoic tectonics. Lithos 356–357, 105350.
Chardon, D., Bamba, O., Traoré, K., 2020. Eburnean deformation pattern of Burkina Faso and the tectonic significance of shear zones in the West African craton. Bulletin de la Société Géologique de France 191.
Chew, D.M., Petrus, J.A., Kamber, B.S., 2014. U-Pb LA–ICPMS dating using accessory mineral standards with variable common Pb. Chem. Geol. 363, 185–199.
Cogné, J.P., 2003. PaleoMac: A Macintosh™ application for treating paleomagnetic data and making plate reconstructions. Geochem. Geophys. Geosyst. 4, 1007.
Cohen, H.A., Gibbs, A.K., 1989. Is the equatorial atlantic discordant? Precambr. Res. 42, 353–369.
Condie, K.C., 1998. Episodic continental growth and supercontinents: a mantle avalanche connection? Earth Planet. Sci. Lett. 163, 97–108.
Condie, K.C., 2002. The supercontinent cycle: are there two patterns of cyclicity? J. Afr. Earth Sc. 35, 179–183.
Condie, K.C., Aster, R.C., 2013. Refinement of the supercontinent cycle with Hf, Nd and Sr isotopes. Geosci. Front. 4, 669–680.
Cordani, U.G., Teixeira, W., 2007. Proterozoic accretionary belts in the Amazonian Craton. Geol. Soc. Am. Mem. 200, 297–320.
Creveling, J.R., Mitrovica, J.X., Chan, N.H., Latychev, K., Matsuyama, I., 2012. Mechanisms for oscillatory true polar wander. Nature 491, 244–248.
D'Agrella Filho, M.S., Trindade, R.I.F., Garcia, M.S.R., Ruiz, A.S., Bispo-Santos, F., Hollanda, M.H., 2018. The Planalto da Serra Alkaline-rock Complex: new 40Ar/39Ar ages and paleomagnetic results, and implications for the Gondwana formation, South American Symposium on Isotope Geology, 11th SSAGI, Cochabamba, Bolivia, p.71.
D'Agrella-Filho, M.S., Trindade, R.I.F., Tohver, E., Janikian, L., Teixeira, W., Hall, C., 2011. Paleomagnetism and 40Ar/39Ar geochronology of the high-grade metamorphic rocks of the Jequié block, São Francisco Craton: Atlantica, Ur and beyond. Precambr. Res. 185, 183–201.
D'Agrella-Filho, M.S., Bispo-Santos, F., Trindade, R.I.F., Antonio, P.Y.J., 2016. Paleomagnetism of the Amazonian Craton and its role in paleocontinents. Braz. J. Geol. 46, 275–299.
Dall'Agnol, R., Lafon, J.M., Macambira, M.J.B., 1994. Proterozoic anorogenic magmatism in the Central Amazonian Province, amazonian araton: Geochronological, petrological and geochemical aspects. Mineral. Petrol. 50, 113–138.
Dall'Agnol, R., Pichavant, M., Champenois, M., 1997. Iron-titanium oxide minerals of the Jamon Granite, eastern Amazonian region, Brazil: implications for the oxygen fugacity in Proterozoic, A-type granites. Anais-Acad. Brasil. De Ciencias 69, 325–348.
Dall'Agnol, R., Teixeira, N.P., Rämö, O.T., Moura, C.A.V., Macambira, M.J.B., de Oliveira, D.C., 2005. Petrogenesis of the Paleoproterozoic rapakivi A-type granites of the Archean Carajás metallogenic province, Brazil. Lithos 80, 101-129.
Dall'Agnol, R., Oliveira, D.C., 2007. Oxidized, magnetite-series, rapakivi-type granites of Carajás, Brazil: Implications for classification and petrogenesis of A-type granites. Lithos 93, 215-233.
Dall'Agnol, R., Oliveira, M.d., Almeida, J.d., Althoff, F., Leite, A.d.S., Oliveira, D., Barros, C., 2006. Archean and paleoproterozoic granitoids of the Carajás Metallogenic Province, eastern Amazonian craton, Symposium on magmatism, crustal evolution and metallogenesis of the Amazoniam Craton, Belém, Excursion Guide, pp. 99–150.
Day, R., Fuller, M., Schmidt, V.A., 1977. Hysteresis properties of titanomagnetites: Grain-size and compositional dependence. Phys. Earth Planet. Inter. 13, 260–267.
De Min, A., Piccirillo, E.M., Marzoli, A., Bellieni, G., Renne, P.R., Ernesto, M., Marques, L. S., 2003. The Central Atlantic Magmatic Province (CAMP) in Brazil: petrology, geochemistry, 40Ar/39Ar ages, paleomagnetism and geodynamic implications. Geophys. Monogr. Ser. 136, 91–128.
De Min, A., Hendriks, B., Slejko, F., Comin-Chiaramonti, P., Girardi, V., Ruberti, E., Gomes, C.B., Neder, R.D., Pinho, F.C., 2013. Age of ultramafic high-K rocks from Planalto da Serra (Mato Grosso, Brazil). J. S. Am. Earth Sci. 41, 57–64.
Di Chiara, A., Muxworthy, A., Trindade, R., Bispo-Santos, F., 2017. Paleoproterozoic geomagnetic field strength from the Avanavero Mafic Sills, Amazonian Craton, Brazil. Geochem. Geophys. Geosyst. 18, 3891–3903.
Dickinson, W.R., Gehrels, G.E., 2003. U-Pb ages of detrital zircons from Permian and Jurassic eolian sandstones of the Colorado Plateau, USA: paleogeographic implications. Sed. Geol. 163, 29–66.
Domeier, M., Van der Voo, R., Torsvik, T.H., 2012. Paleomagnetism and Pangea: the road to reconciliation. Tectonophys. 514–517, 14–43.
Donadini, F., Elming, S.-Å., Tauxe, L., Hålenius, U., 2011. Paleointensity determination on a 1.786Ga old gabbro from Hoting, Central Sweden. Earth Planet. Sci. Lett. 309, 234–248.
Dunlop, D.J., Argyle, K.S., 1991. Separating multidomain and single-domain-like remanences in pseudo-single-domain magnetites (215–540 nm) by low-temperature demagnetization. J. Geophys. Res. Solid Earth 96, 2007–2017.
Dunlop, D.J., Özdemir, Ö., 2000. Effect of grain size and domain state on thermal demagnetization tails. Geophys. Res. Lett. 27, 1311–1314.
Ernst, R., Srivastava, R., Bleeker, W., Hamilton, M., 2010. Precambrian Large Igneous Provinces (LIPs) and their dyke swarms: New insights from high-precision geochronology integrated with paleomagnetism and geochemistry. Precambr. Res. 183, vii–xi.
Ernst, R.E., Bleeker, W., Söderlund, U., Kerr, A.C., 2013. Large Igneous Provinces and supercontinents: Toward completing the plate tectonic revolution. Lithos 174, 1–14.
Ernst, R.E., 2014. Large Igneous Provinces. Cambridge University Press, p. 304.
Ernst, W.G., 2017. Earth's thermal evolution, mantle convection, and Hadean onset of plate tectonics. J. Asian Earth Sci. 145, 334–348.
Evans, D.A.D., Mitchell, R.N., 2011. Assembly and breakup of the core of Paleoproterozoic-Mesoproterozoic supercontinent Nuna. Geology 39, 443–446.
Evans, D.A.D., 2013. Reconstructing pre-Pangean supercontinents. Geol. Soc. Am. Bull. 125, 1735–1751.
Evans, D.A.D., Li, Z.-X., Murphy, J.B., 2016. Four-dimensional context of Earth's supercontinents. Geological Society, London, Special Publications 424, 1–14.
Evans, M.E., Bingham, D.K., 1976. Paleomagnetism of the Great Slave Supergroup, Northwest Territories, Canada: the Tochatwi Formation. Can. J. Earth Sci. 13, 555–562.
Fernandes, C.M.D., Juliani, C., Monteiro, L.V.S., Lagler, B., Echeverri Misas, C.M., 2011. High-K calc-alkaline to A-type fissure-controlled volcano-plutonism of the São Félix do Xingu region, Amazonian craton, Brazil: exclusively crustal sources or only mixed Nd model ages? J. S. Am. Earth Sci. 32, 351–368.
Feybesse, J.-L., Milési, J.-P., 1994. The Archaean/Proterozoic contact zone in West Africa: a mountain belt of décollement thrusting and folding on a continental margin related to 2.1 Ga convergence of Archaean cratons? Precambr. Res. 69, 199–227.
Fisher, R., 1953. Dispersion on a sphere. Proc. R. Soc. Lond. A 217, 295–305.
Garcia, M.S., Trindade, R.I., Manoel, S., Pinho, F.E., 2013. Paleomagnetismo do complexo alcalino Planalto da Serra (Mato Grosso): Implicações para a formação do Gondwana, In: Letters, L. (Ed.), Latinmag Letters, Montevideo, pp. OB19, 11-18.
Giovanardi, T., Girardi, V.A.V., Teixeira, W., Mazzucchelli, M., 2019. Mafic dyke swarms at 1882, 535 and 200 Ma in the Carajás region, Amazonian Craton: SrNd isotopy, trace element geochemistry and inferences on their origin and geological settings. J. S. Am. Earth Sci. 92, 197–208.
Goldreich, P., Toomre, A., 1969. Some remarks on polar wandering. J. Geophys. Res. 74, 2555–2567.
Gong, Z., Xu, X., Evans, D.A.D., Hoffman, P.F., Mitchell, R.N., Bleeker, W., 2018. Paleomagnetism and rock magnetism of the ca. 1.87 Ga Pearson Formation, Northwest Territories, Canada: a test of vertical-axis rotation within the Great Slave basin. Precambr. Res. 305, 295–309.
Grenholm, M., 2019. The global tectonic context of the ca. 2.27-1.96 Ga Birimian Orogen – insights from comparative studies, with implications for supercontinent cycles. Earth Sci. Rev. 193, 260–298.
Halls, H.C., 1978. The use of converging remagnetization circles in palaeomagnetism. Phys. Earth Planet. Inter. 16, 1–11.
Hanson, R.E., Gose, W.A., Crowley, J.L., Ramezani, J., Bowring, S.A., Bullen, D.S., Hall, R.P., Pancake, J.A., Mukwakwami, J., 2004. Paleoproterozoic intraplate magmatism and basin development on the Kaapvaal Craton: age, paleomagnetism and geochemistry of ~1.93 to ~1.87 Ga post-Waterberg dolerites. S. Afr. J. Geol. 107, 233–254.
Hanson, R.E., Rioux, M., Gose, W.A., Blackburn, T.J., Bowring, S.A., Mukwakwami, J., Jones, D.L., 2011. Paleomagnetic and geochronological evidence for large-scale post–1.88 Ga displacement between the Zimbabwe and Kaapvaal cratons along the Limpopo belt. Geology 39, 487–490.
Hyodo, H., Dunlop, D.J., 1993. Effect of anisotropy on the paleomagnetic contact test for a Grenville Dike. J. Geophys. Res. Solid Earth 98, 7997–8017.
Isley, A.E., Abbott, D.H., 1999. Plume-related mafic volcanism and the deposition of banded iron formation. J. Geophys. Res. Solid Earth 104, 15461–15477.
Johansson, Å., 2009. Baltica, Amazonia and the SAMBA connection—1000 million years of neighbourhood during the Proterozoic? Precambr. Res. 175, 221–234.
Juliani, C., Fernandes, C.M.D., 2010. Well-preserved Late Paleoproterozoic volcanic centers in the São Félix do Xingu region, Amazonian Craton, Brazil. J. Volcanol. Geoth. Res. 191, 167–179.
Kilian, T.M., Chamberlain, K.R., Evans, D.A.D., Bleeker, W., Cousens, B.L., 2016. Wyoming on the run—Toward final Paleoproterozoic assembly of Laurentia. Geology 44, 863–866.
Kirschvink, J.L., 1980. The least-squares line and plane and the analysis of palaeomagnetic data. Geophys. J. Int. 62, 699–718.
Kirschvink, J.L., Ripperdan, R.L., Evans, D.A., 1997. Evidence for a large-scale reorganization of Early Cambrian continental masses by inertial interchange true polar wander. Science 277, 541–545.
Kirschvink, J.L., Kopp, R.E., Raub, T.D., Baumgartner, C.T., Holt, J.W., 2008. Rapid, precise, and high-sensitivity acquisition of paleomagnetic and rock-magnetic data: Development of a low-noise automatic sample changing system for superconducting rock magnetometers. Geochemistry Geophysics. Geosys. 9.
Klein, E.L., Moura, C.A.V., 2008. São Luís Craton and Gurupi Belt (Brazil): possible links with the West African Craton and surrounding Pan-African belts. Geological Society, London, Special Publications 294, 137–151.
Kruiver, P.P., Dekkers, M.J., Heslop, D., 2001. Quantification of magnetic coercivity components by the analysis of acquisition curves of isothermal remanent magnetisation. Earth Planet. Sci. Lett. 189, 269–276.
Ledru, P., Lasserre, J.-L., Manier, E., Mercier, D., 1991. Le Protérozoïque inférieur nord guyanais: révision de la lithologie, tectonique transcurrente et dynamique des bassins sédimentaires. Bull. Soc. Géol. France 162, 627–636.
Ledru, P., Johan, V., Milési, J.P., Tegyey, M., 1994. Markers of the last stages of the Palaeoproterozoic collision: evidence for a 2 Ga continent involving circum-South Atlantic provinces. Precambr. Res. 69, 169–191.
Li, Z.-X., Evans, D.A.D., Halverson, G.P., 2013. Neoproterozoic glaciations in a revised global palaeogeography from the breakup of Rodinia to the assembly of Gondwanaland. Sed. Geol. 294, 219–232.
Liu, H., Sun, W.-D., Zartman, R., Tang, M., 2019. Continuous plate subduction marked by the rise of alkali magmatism 2.1 billion years ago. Nat. Commun. 10, 3408.
Liu, Y., Li, Z.-X., Pisarevsky, S., Kirscher, U., Mitchell, R.N., Stark, J.C., 2018. Palaeomagnetism of the 1.89 Ga Boonadgin dykes of the Yilgarn Craton: Possible connection with India. Precambr. Res. 329, 211–223.

Lubnina, N.V., Pasenko, A.M., Novikova, M.A., Bubnov, A.Y., 2016. The East European craton at the end of the Paleoproterozoic: a new paleomagnetic pole of 1.79–1.75 Ga. Moscow Univ. Geol. Bull. 71, 8–17.
Ludwig, K., 2009. Isoplot 4.1. A geochronological toolkit for Microsoft Excel. Berkeley Geochronology Center Special Publication 4, 76.
McDowell, F.W., McIntosh, W.C., Farley, K.A., 2005. A precise 40Ar–39Ar reference age for the Durango apatite (U–Th)/He and fission-track dating standard. Chem. Geol. 214, 249–263.
McElhinny, M., 1964. Statistical significance of the fold test in palaeomagnetism. Geophys. J. Int. 8, 338–340.
McFadden, P.L., McElhinny, M.W., 1990. Classification of the reversal test in palaeomagnetism. Geophys. J. Int. 103, 725–729.
McGlynn, J.C., Irving, E., 1978. Multicomponent magnetization of the Pearson Formation (Great Slave Supergroup, N.W.T.) and the Coronation loop. Can. J. Earth Sci. 15, 642–654.
Meert, J.G., 2012. What's in a name? the Columbia (Paleopangaea/Nuna) supercontinent. Gondwana Res. 21, 987–993.
Meert, J.G., Santosh, M., 2017. The Columbia supercontinent revisited. Gondwana Res. 50, 67–83.
Merdith, A.S., Collins, A.S., Williams, S.E., Pisarevsky, S., Foden, J.F., Archibald, D., Blades, M.L., Alessio, B.L., Armistead, S., Plavsa, D., Clark, C., Müller, R.D., 2017. A full-plate global reconstruction of the Neoproterozoic. Gondwana Res.
Mitchell, R.N., Hoffman, P.F., Evans, D.A.D., 2010. Coronation loop resurrected: Oscillatory apparent polar wander of Orosirian (2.05–1.8Ga) paleomagnetic poles from Slave craton. Precambr. Res. 179, 121–134.
Mitchell, R.N., 2014. True polar wander and supercontinent cycles: Implications for lithospheric elasticity and the triaxial earth. Am. J. Sci. 314, 966–979.
Moreira, G., 2019. Paleomagnetismo Da Formação Penatecaua Da Província Magmática Do Atlântico Central Na Bacia Amazônica, brasil, Instituto de Astronomia, Geofísica e Ciências Atmosféricas - Departamento de Geofísica. University of São Paulo, p. 63.
Murphy, J.B., 2013. Whither the supercontinent cycle? Geology 41, 815–816.
Nance, D., Worsley, T.R., Moody, J.B., 1988. The supercontinent cycle. Sci. Am. 259, 72–79.
Nance, D., Murphy, J.B., 2013. Origins of the supercontinent cycle. Geosci. Front. 4, 439–448.
Nance, R.D., Murphy, J.B., Santosh, M., 2014. The supercontinent cycle: a retrospective essay. Gondwana Res. 25, 4–29.
Navarro, M., Tonetto, E., Oliveira, E., 2015. LA-SF-ICP-MS U-Pb Zircon Dating at University of Campinas, Brazil. Geonalysis-2015, Wien, August.
Nédélec, A., Bouchez, J.-L., 2015. Granites: Petrology, Structure, Geological Setting, and Metallogeny. OUP Oxford.
Nédélec, A., Trindade, R., Peschler, A., Archanjo, C., Macouin, M., Poitrasson, F., Bouchez, J.-L., 2015. Hydrothermally-induced changes in mineralogy and magnetic properties of oxidized A-type granites. Lithos 212–215, 145–157.
Neres, M., Silva, P.F., Ikenne, M., Martins, S., Hafid, A., Mata, J., Almeida, F., Youbi, N., Boumehdi, M.A., 2016. Evidences for multiple remagnetization of Proterozoic dykes from Iguerda inlier (Anti-Atlas Belt, Southern Morocco). Stud Geophys Geod 60, 700–730.
Nomade, S., Théveniaut, H., Chen, Y., Pouclet, A., Rigollet, C., 2000. Paleomagnetic study of French Guyana Early Jurassic dolerites: hypothesis of a multistage magmatic event. Earth Planet. Sci. Lett. 184, 155–168.
Nomade, S., Chen, Y., Féraud, G., Pouclet, A., Théveniaut, H., 2001. First paleomagnetic and 40Ar/39Ar study of Paleoproterozoic rocks from the French Guyana (Camopi and Oyapok rivers), northeastern Guyana Shield. Precambr. Res. 109, 239–256.
Nomade, S., Chen, Y., Pouclet, A., Féraud, G., Théveniaut, H., Daouda, B.Y., Vidal, M., Rigolet, C., 2003. The Guiana and the West African Shield Palaeoproterozoic grouping: new palaeomagnetic data for French Guiana and the Ivory Coast. Geophys. J. Int. 154, 677–694.
Oliveira, D.C., 2006. Modelos de evolução e colocação dos grantitos paleoproterozóicos da Suíte Jamon, SE do Cráton Amazônico. Tese de douturado. Universidade Federal do Pará, p.186.
Onstott, T., Hargraves, R.B., 1981. Proterozoic transcurrent tectonics: palaeomagnetic evidence from Venezuela and Africa. Nature 289, 131–136.
Onstott, T., Hargraves, R., York, D., 1984a. Dating of Precambrian diabase dikes of Venezuela using paleomagnetic and 40Ar/39Ar methods. Anais II do Simpósio Amazônico, Manaus, Brasil, DNPM 2, 513–518.
Onstott, T., Hargraves, R.B., York, D., Hall, C., 1984b. Constraints on the motions of South American and African Shields during the Proterozoic: I. 40Ar/39Ar and paleomagnetic correlations between Venezuela and Liberia. Geol. Soc. Am. Bull. 95, 1045–1054.
Onstott, T.C., Dorbor, J., 1987. 40Ar/39Ar and paleomagnetic results from Liberia and the Precambrian APW data base for the West African Shield. J. Afr. Earth Sc. 1983 (6), 537–552.
Paquette, J.-L., Piro, J.-L., Devidal, J.-L., Bosse, V., Didier, A., Sannac, S., Abdelnour, Y., 2014. Sensitivity enhancement in LA-ICP-MS by N2 addition to carrier gas: application to radiometric dating of U-Th-bearing minerals. Agilent ICP-MS J. 58, 4–5.
Paton, C., Hellstrom, J., Paul, B., Woodhead, J., Hergt, J., 2011. Iolite: Freeware for the visualisation and processing of mass spectrometric data. J. Anal. At. Spectrom. 26, 2508–2518.
Pehrsson, S.J., Eglington, B.M., Evans, D.A.D., Huston, D., Reddy, S.M., 2016. Metallogeny and its link to orogenic style during the Nuna supercontinent cycle. Geological Soc., London, Special Publ. 424, 83–94.
Peucat, J.-J., Capdevila, R., Drareni, A., Mahdjoub, Y., Kahoui, M., 2005. The Eglab massif in the West African Craton (Algeria), an original segment of the Eburnean orogenic belt: petrology, geochemistry and geochronology. Precambr. Res. 136, 309–352.
Pimentel, M., Machado, N., 1994. Geocronologia U-Pb dos terrenos granito-greenstone de Rio Maria, Pará, SBG, Congresso Brasileiro de Geologia, pp. 390–391.
Pinho, S., Fernandes, C., Teixeira, N., Paiva Jr, A., Cruz, V., Lamarão, C., Moura, C., 2006. O magmatismo paleoproterozóico da região de São Félix do Xingu, Província Estanífera do sul do Pará: Petrografia e Geocronologia. Rev. Brasil. Geoci. 36, 724–732.
Piper, J.D.A., Lomax, K., 1973. Palaeomagnetism of Precambrian Birrimian and Tarkwaian Rocks of West Africa. Geophys. J. Int. 34, 435–450.
Pisarevsky, S.A., Elming, S.-Å., Pesonen, L.J., Li, Z.-X., 2014. Mesoproterozoic paleogeography: Supercontinent and beyond. Precambr. Res. 244, 207–225.
Pivarunas, A.F., Meert, J.G., Miller, S.R., 2018. Assessing the intersection/remagnetization puzzle with synthetic apparent polar wander paths. Geophys. J. Int. 214, 1164–1172.
Pochon, A., Poujol, M., Gloaguen, E., Branquet, Y., Cagnard, F., Gumiaux, C., Gapais, D., 2016. U-Pb LA-ICP-MS dating of apatite in mafic rocks: Evidence for a major magmatic event at the Devonian-Carboniferous boundary in the Armorican Massif (France). Am. Mineral. 101, 2430–2442.
Raub, T., Kirschvink, J., Evans, D., 2007. True polar wander: Linking deep and shallow geodynamics to hydro-and bio-spheric hypotheses. Treat. Geophys. 5, 565–589.
Renne, P., Onstott, T., Jorge João, X., 1988. 40Ar/39Ar and paleomagnetic results from the Guaporé Shield: further implications for the nature of Middle-Late Proterozoic mobile belts of Gondwanaland. SBG, Congr. Lat.-Amer Geol 7, 348–362.
Rivalenti, G., Williamson, A., Feyer, A.M., Mazzucchelli, M., Girardi, V.A.V., Cavazzini, G., Finatti, C., Barbieri, M.A., Teixeira, W., 1998. Petrogenesis of the Paleoproterozoic basalt-andesite-rhyolite dyke association in the Carajas region, Amazonian craton. Lithos 43, 235-265.
Roberts, A.P., Heslop, D., Zhao, X., Pike, C.R., 2014. Understanding fine magnetic particle systems through use of first-order reversal curve diagrams. Rev. Geophys. 52, 557–602.
Roberts, A.P., Almeida, T.P., Church, N.S., Harrison, R.J., Heslop, D., Li, Y., Li, J., Muxworthy, A.R., Williams, W., Zhao, X., 2017. Resolving the Origin of Pseudo-Single Domain Magnetic Behavior. J. Geophys. Res. Solid Earth 122, 9534–9558.
Roberts, N.M.W., 2013. The boring billion? - Lid tectonics, continental growth and environmental change associated with the Columbia supercontinent. Geosci. Front.
Rodrigues, P.R.S., Lamarão, C.N., da Costa, H.d.N.S., Oliveira, D.C., Galarza, M.A., Sotero, A.d.M., 2015. Petrografia, geoquímica e geocronologia de diques máficos a félsicos da região de Água Azul do Norte, sudeste do Pará, Província Carajás. Bol. Mus. Para. Emílio Goeldi. Cienc. Nat Belém 10, 311–339.
Rosa-Costa, L.T., Lafon, J.M., Delor, C., 2006. Zircon geochronology and Sm–Nd isotopic study: Further constraints for the Archean and Paleoproterozoic geodynamical evolution of the southeastern Guiana Shield, north of Amazonian Craton, Brazil. Gondwana Res. 10, 277–300.
Rose, I., Buffett, B., 2017. Scaling rates of true polar wander in convecting planets and moons. Phys. Earth Planet. Inter. 273, 1–10.
Roverato, M., 2016. The Montesbelos mass-flow (southern Amazonian craton, Brazil): a Paleoproterozoic volcanic debris avalanche deposit? Bull. Volcanol. 78, 1–6.
Roverato, M., Giordano, D., Giovanardi, T., Juliani, C., Polo, L., 2019. The 2.0–1.88 Ga Paleoproterozoic evolution of the southern Amazonian Craton (Brazil): An interpretation inferred by lithofaciological, geochemical and geochronological data. Gondwana Res.
Sabaté, P., Lomax, K., 1975. Données stratigraphiques et paléomagnétiques de la région Yetti-Eglab (Sahara occidental algérien).
Santos, J.O.S., Hartmann, L.A., Gaudette, H.E., Groves, D.I., McNaughton, N.J., Fletcher, I.R., 2000. A new understanding of the provinces of the Amazon Craton Based on Integration of Field Mapping and U-Pb and Sm-Nd Geochronology. Gondwana Res. 3, 453–488.
Santos, J.O.S., 2003. Geotectônica do Escudo das Guianas e Brasil-Central, Geologia, Tectônica e Recursos Minerais do Brasil. Texto, mapas & SIG: CPRM—Serviço Geológico do Brasil, pp. 169-226.
Santos, M.N.S.d., Oliveira, D.C., 2016. Rio Maria granodiorite and associated rocks of Ourilândia do Norte – Carajás province: Petrography, geochemistry and implications for sanukitoid petrogenesis. J. South Am. Earth Sci. 72, 279–301.
Schobbenhaus, C., Campos, D.A., Derze, G.R., Asmus, H.E., 1984. Geologia do Brasil: Texto Explicativo do mapa Geológico do Brasil e da Área Oceânica Adjacente Incluindo Depósitos Minerais, escala 1: 2 5000 000. Divisão de Geologia e Mineralogia, Departamento Nacional da Produção Mineral.
Schoene, B., Bowring, S.A., 2006. U-Pb systematics of the McClure Mountain syenite: thermochronological constraints on the age of the 40 Ar/39 Ar standard MMhb. Contrib Mineral Petrol 151, 615.
Shcherbakova, V.V., Shcherbakov, V.P., Heider, F., 2000. Properties of partial thermoremanent magnetization in pseudosingle domain and multidomain magnetite grains. J. Geophys. Res. Solid Earth 105, 767–781.
Shirey, S.B., Richardson, S.H., 2011. Start of the Wilson Cycle at 3 Ga Shown by Diamonds from Subcontinental Mantle. Science 333, 434–436.
Silva, C., Lima, M.d., Andrade, A.d., Isler, R., Guimarães, G., Leal, J., Basei, M., D'lagnol, R., Teixeira, J., Montalvão, R., 1974. Folha SB-22 (Araguaia) e parte da Folha SC-22 (Tocantins). Projeto RadamBrasil, 143.
Silva, F.F., de Oliveira, D.C., Antonio, P.Y.J., D'Agrella Filho, M.S., Lamarão, C.N., 2016. Bimodal magmatism of the Tucumã area, Carajás province: U-Pb geochronology, classification and processes. J. S. Am. Earth Sci. 72, 95–114.
Silva Jr, R., Dall'Agnol, R., Oliveira, E., 1999. Geologia, petrografia e geoquímica dos diques proterozóicos da região de Rio Maria, sudeste do Pará. Geochim. Brasil. 13, 161–183.

Söderlund, U., Klausen, M.B., Ernst, R.E., Bleeker, W., 2016. New advances in using large igneous provinces (LIPs) to reconstruct ancient supercontinents. GFF 138, 1–5.
Stacey, J.S., Kramers, J.D., 1975. Approximation of terrestrial lead isotope evolution by a two-stage model. Earth Planet. Sci. Lett. 26, 207–221.
Stampfli, G.M., Hochard, C., Vérard, C., Wilhem, C., vonRaumer, J., 2013. The Formation of Pangea. Tectonophysics 593, 1–19.
Stark, J.C., Wang, X.-C., Denyszyn, S.W., Li, Z.-X., Rasmussen, B., Zi, J.-W., Sheppard, S., Liu, Y., 2019. Newly identified 1.89 Ga mafic dyke swarm in the Archean Yilgarn Craton, Western Australia suggests a connection with India. Precambr. Res. 329, 156–169.
Swanson-Hysell, N.L., Kilian, T.M., Hanson, R.E., 2015. A new grand mean palaeomagnetic pole for the 1.11 Ga Umkondo large igneous province with implications for palaeogeography and the geomagnetic field. Geophys. J. Int. 203, 2237–2247.
Tassinari, C.C., Munhá, J.M., Teixeira, W., Palácios, T., Nutman, A.P., Sosa, C., Santos, A. P., Calado, B.O., 2004. The Imataca Complex, NW Amazonian Craton, Venezuela: crustal evolution and integration of geochronological and petrological cooling histories. Episodes-Newsmag. Int. Union Geol. Sci. 27 (1), 3–12.
Tassinari, C.C.G., Macambira, M., 2004. A evolução tectonica do Craton Amazonico, In: (Org.), V.M.-N.A.B.C.D.R.C.B.B.d.B.N. (Ed.), Geologia do Continente Sul Americano: Evolução da obra de F.F.M. de Ameida. BECA, São Paulo, pp. p. 471–486.
Teixeira, M.F.B., Dall'Agnol, R., Schneider Santos, J.O., Carvalho de Oliveira, D., Lamarão, C.N., McNaughton, N.J., 2018. Crystallization ages of Paleoproterozoic A-type granites of Carajás province, Amazon craton: Constraints from U-Pb geochronology of zircon and titanite. J. South Am. Earth Sci. 88, 312–331.
Teixeira, M.F.B., Dall'Agnol, R., Santos, J.O.S., Kemp, A., Evans, N., 2019a. Petrogenesis of the Paleoproterozoic (Orosirian) A-type granites of Carajás Province, Amazon Craton, Brazil: Combined in situ HfO isotopes of zircon. Lithos 332–333, 1–22.
Teixeira, W., Hamilton, M.A., Ernst, R.E., Girardi, V.A.V., 2012a. 200 Ma dyke swarm in the Carajás province, Amazonian craton, South America: distal part of the CAMP event, Reconstruction of Supercontinents Back To 2.7 Ga Using The Large Igneous Province (LIP) Record: With Implications For Mineral Deposit Targeting, Hydrocarbon Resource Exploration, and Earth System Evolution.
Teixeira, W., Hamilton, M.A., Ernst, R.E., Girardi, V.A.V., Evans, D.A.D., 2012b. 535 Ma dyke swarm in the Carajás province, Amazonian craton, South America: potential part of a regional intraplate event, Reconstruction of Supercontinents Back To 2.7 Ga Using The Large Igneous Province (LIP) Record: With Implications For Mineral Deposit Targeting, Hydrocarbon Resource Exploration, and Earth System Evolution, pp. 1–11.
Teixeira, W., Hamilton, M., Girardi, V.A.V., Faleiros, F.M., Ernst, R.E., 2019b. U-Pb baddeleyite ages of key dyke swarms in the Amazonian Craton (Carajás/Rio Maria and Rio Apa areas): tectonic implications for events at 1880, 1110 Ma, 535 Ma and 200 Ma. Precambr. Res. 329, 138–155.
Théveniaut, H., Delor, C., Lafon, J.M., Monié, P., Rossi, P., Lahondère, D., 2006. Paleoproterozoic (2155–1970 Ma) evolution of the Guiana Shield (Transamazonian event) in the light of new paleomagnetic data from French Guiana. Precambrian Res. 150, 221–256.
Thomson, S.N., Gehrels, G.E., Ruiz, J., Buchwaldt, R., 2012. Routine low-damage apatite U-Pb dating using laser ablation–multicollector–ICPMS. Geochemistry, Geophysics, Geosystems 13.
Trindade, R.I.F., Font, E., D'Agrella-Filho, M.S., Nogueira, A.C.R., Riccomini, C., 2003. Low-latitude and multiple geomagnetic reversals in the Neoproterozoic Puga cap carbonate, Amazon craton. Terra Nova 15, 441–446.
Valério, C.d.S., Macambira, M.J.B., Souza, V.d.S., Dantas, E.L., Nardi, L.V.S., 2018. 1.88Ga São Gabriel AMCG association in the southernmost Uatumã-Anauá Domain: Petrological implications for post-collisional A-type magmatism in the Amazonian Craton. Lithos 300–301, 291–313.
Van der Voo, R., 1990. The reliability of paleomagnetic data. Tectonophysics 184, 1–9.
Vanderhaeghe, O., Ledru, P., Thiéblemont, D., Egal, E., Cocherie, A., Tegyey, M., Milési, J.-P., 1998. Contrasting mechanism of crustal growth: Geodynamic evolution of the Paleoproterozoic granite–greenstone belts of French Guiana. Precambr. Res. 92, 165–193.
Vasquez, L., Rosa-Costa, L., Silva, C., Ricci, P., Barbosa, J., Klein, E., Lopes, E., Macambira, E., Chaves, C., Carvalho, J., 2008. Geologia e Recursos Minerais do Estado do Pará: Sistema de Informações Geográficas-SIG: texto explicativo dos mapas Geológico e Tectônico e de Recursos Minerais do Estado do Pará. Organizadores, Vasquez ML, Rosa-Costa LT Escala 1, 000.
Veikkolainen, T., Pesonen, L., Korhonen, K., 2014. An analysis of geomagnetic field reversals supports the validity of the Geocentric Axial Dipole (GAD) hypothesis in the Precambrian. Precam. Res. 244, 33–41.
Veikkolainen, T., Heimpel, M., Evans, M.E., Pesonen, L.J., Korhonen, K., 2017a. A paleointensity test of the geocentric axial dipole (GAD) hypothesis. Phys. Earth Planet. Inter. 265, 54–61.
Veikkolainen, T.H., Biggin, A.J., Pesonen, L.J., Evans, D.A., Jarboe, N.A., 2017b. Advancing Precambrian palaeomagnetism with the PALEOMAGIA and PINT((QPI)) databases. Sci. Data 4.
Veselovskiy, R.V., Samsonov, A.V., Stepanova, A.V., Salnikova, E.B., Larionova, Y.O., Travin, A.V., Arzamastsev, A.A., Egorova, S.V., Erofeeva, K.G., Stifeeva, M.V., Shcherbakova, V.V., Shcherbakov, V.P., Zhidkov, G.V., Zakharov, V.S., 2019. 1.86 Ga key paleomagnetic pole from the Murmansk craton intrusions – Eastern Murman Sill Province, NE Fennoscandia: Multidisciplinary approach and paleotectonic applications. Precambrian Res. 324, 126–145.
Warnock, A.C., Kodama, K.P., Zeitler, P.K., 2000. Using thermochronometry and low-temperature demagnetization to accurately date Precambrian paleomagnetic poles. J. Geophys. Res. Solid Earth 105, 19435–19453.
Whitney, D.L., Evans, B.W., 2010. Abbreviations for names of rock-forming minerals. Am. Mineralo. 95, 185–187.
Wiedenbeck, M., Alle, P., Corfu, F., Griffin, W., Meier, M., Oberli, F.V., Quadt, A.V., Roddick, J., Spiegel, W., 1995. Three natural zircon standards for U-Th-Pb, Lu-Hf, trace element and REE analyses. Geostand. Newslett. 19, 1–23.
Worsley, T.R., Nance, D., Moody, J.B., 1984. Global tectonics and eustasy for the past 2 billion years. Mar. Geol. 58, 373–400.
Zhang, S., Li, Z.-X., Evans, D.A.D., Wu, H., Li, H., Dong, J., 2012. Pre-Rodinia supercontinent Nuna shaping up: a global synthesis with new paleomagnetic results from North China. Earth Planet. Sci. Lett. 353–354, 145–155.
Zhao, G., Sun, M., Wilde, S.A., 2002. Did South America and West Africa Marry and Divorce or Was it a Long-lasting Relationship? Gondwana Res. 5, 591–596.
Zhao, G., Sun, M., Wilde, S.A., Li, S., 2004. A Paleo-Mesoproterozoic supercontinent: assembly, growth and breakup. Earth Sci. Rev. 67, 91–123.
Zijderveld, J., 1967. AC demagnetization of rocks: analysis of results. Methods Paleomagn. 3, 254.